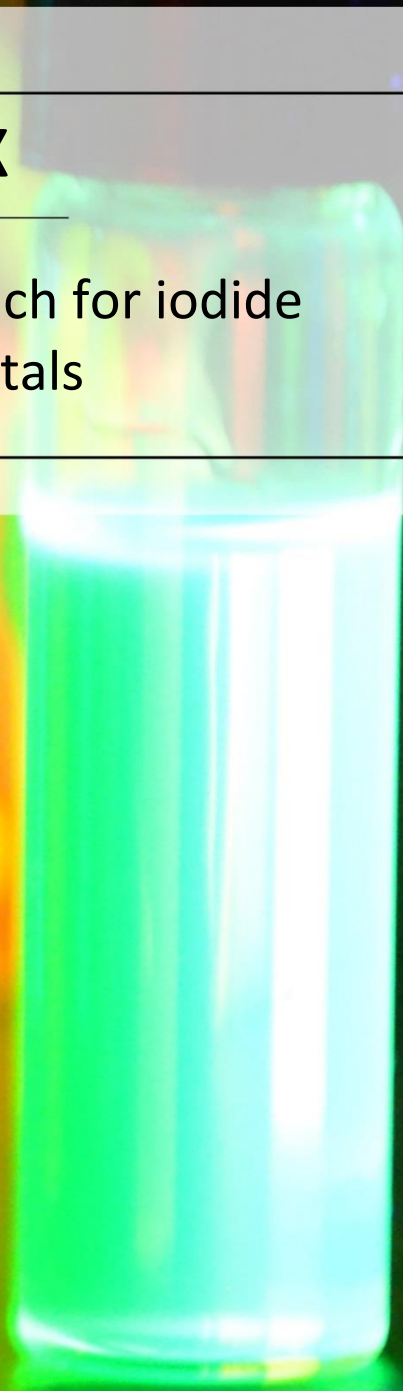




Chapter X

A novel synthesis approach for iodide based nanocrystals



Chapter X: A Novel synthesis approach for iodide based nanocrystals*

Abstract: In this chapter, the synthesis of various binary and ternary inorganic and hybrid organic-inorganic iodide NCs starting from molecular iodine will be discussed. The synthesis described herein utilizes a reaction between I_2 and oleylamine, which results in oleylammonium iodide - an iodide precursor that can be directly used in the preparation of iodide based NCs. The versatility of this synthesis was demonstrated by synthesizing various different types of nanocrystals: KI, RbI, CsI, AgI, CsPbI₃, FAPbI₃, Cs₄PbI₆, Cs₃Bi₂I₉, FA₃Bi₂I₉ and RbAg₄I₅. Furthermore, the syntheses are easy and are carried out in vials that are heated on a hotplate in air. They exhibit not only narrow size distributions, but also, in the case of lead-based perovskites nanocrystals, 70-80% photoluminescence quantum yields.

10.1 Introduction

Metal halide NCs have gained increasing attention over the past few years.¹⁻³ Among these, the LHP NCs are by far the most studied ones due to their excellent optical properties and relatively simple synthesis methods.^{1-2, 4} The great interest in these NCs has also motivated the development of synthesis approaches for other colloidal halide based NCs. The search for other colloidal halide based NCs is mainly driven by the search for lead-free perovskite alternatives to the Pb-based ones. This has led, for instance, to reports on the synthesis of ternary Cs₂SnI₆, Cs₃Bi₂X₉ and Cs₃Sb₂X₉ NCs, and quaternary Cs₂AgBiX₆ double perovskite NCs.⁵⁻⁹ Other groups of new metal halide NCs that have emerged from perovskite NC research are Cs₄PbX₆ NCs and simple cesium halide NCs which are appealing due to their interesting transformation reactions.¹⁰⁻¹¹

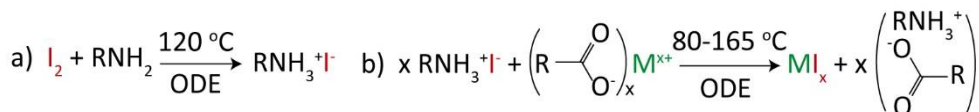
The vast majority of colloidal metal halide NCs are now prepared based on the CsPbX₃ NC colloidal synthesis scheme that was first reported by Protesescu *et al.*;¹ a Cs-oleate solution is quickly injected into a hot solution of a metal halide precursor (for example PbX₂) that has previously been dissolved in octadecene (ODE), OLAM (OLAM) and OA (OA). Although this method yields high quality perovskite NCs, it does not allow the Pb:halide molar ratio that was introduced in the synthesis to be controlled. Moreover, it relies strongly on the solubility of the metal halide precursors in the ligand/solvent mixture. Furthermore, this method cannot be generalized, as many metal halides (for example AgBr and PbCl₂) are difficult to dissolve in simple OA and OLAM mixtures, and additional ligands (such as trioctyl phosphine oxide) are required.^{1, 12} The high cost and instability of certain metal halide salts, as is the case for most transition metal iodides, are also problematic. These precursors are often highly reactive, and not much work has been done with regard to controlling the precursor reactivity, as opposed to the extensive research that has been devoted to identifying suitable chemicals for the synthesis of the more traditional cadmium

*Based on: Molecular Iodine for a General Synthesis of Binary and Ternary Inorganic and Hybrid Organic-Inorganic Iodide Nanocrystals. Quinten A. Akkerman, Laura Martínez-Sarti, Luca Goldoni, Muhammad Imran, Dmitry Baranov, Henk J. Bolink, Francisco Palazon and Liberato Manna. *Chemistry of Materials*, 30, 6915–6921 (2018). Copyright © 2018 American Chemical Society

and lead chalcogenide NCs.¹³⁻¹⁴ Developing synthetic methods in which elemental ratios, especially between cations and anions, can be tuned independently is an important goal in the preparation of multinary materials, and this is also relevant to metal halide perovskites. To this end, Creutz *et al.*, Imran *et al.* and Krieg *et al.* recently reported a different method of preparing metal halide NCs, in which a reactive halide precursor (trimethylsilyl halide, benzoyl halide or trioctylphosphine halide) is injected into a solution of metal acetate salts.¹⁵⁻¹⁷ Imran *et al.*, for example, demonstrated that this synthesis can be extended to various perovskite APbX₃ NCs by simply choosing the proper precursors and optimizing the reaction conditions.¹⁶ Although the use of trimethylsilyl halides or benzoyl halides resulted in perovskite and double perovskite NCs with narrow size distributions, these chemicals are air sensitive, which prevents them from being used in syntheses that are conducted under ambient conditions (i.e. in air).

In this chapter, a general synthesis of binary and ternary inorganic and hybrid organic-inorganic iodide NCs is described. These NCs are synthesized via the injection of an OLAM-I₂ solution into an ODE solution containing metal and organic oleates, as shown in **scheme 10.1**. *Section 10.2* will describe the synthesis of the oleylammonium iodide precursor. By choosing the appropriate metal or organic salt precursor, and optimizing the OA concentration and reaction temperature, inorganic and hybrid organic-inorganic iodide NCs with various different compositions. The nearly monodisperse lead iodide perovskite NCs, as discussed in *section 10.3*, had photoluminescence quantum yields (PLQYs) close to 80% and a good stability over at least several weeks in air. Furthermore, NCs such as CsI RbI, KI, could easily be synthesized, as shown in *section 10.4*. The synthesis could also be extended to bismuth based NCs like FA₃Bi₂I₉ and Cs₃Bi₂I₉, which are discussed in *section 10.5*. Finally, the synthesis could be used for the synthesis of silver base iodide NCs like AgI and RbAg₄I₅ which is described in *section 10.6*.

Scheme 10.1. Reactio of I₂ with oleylamine. (a) *In situ* synthesis of oleylammonium iodide starting from iodine and OLAM. **(b)** General synthesis of metal iodide NCs, in which the oleylammonium iodide precursor is injected into an octadecene solution containing metal oleates.



MI = KI, RbI, CsI, AgI, CsPbI₃, FAPbI₃, Cs₄PbI₆, Cs₃Bi₂I₉, FA₃Bi₂I₉, RbAg₄I₅ R = oleyl

10.2 In situ synthesis of oleylammonium iodide

The iodide precursor that was used in the synthesis of the various NCs reported here was prepared by heating solid grains of molecular I₂ in a solution of ODE and OLAM, as is depicted in reaction **scheme 10.1a**. This led to the *in situ* formation of oleylammonium iodide (see **figure 10.1a**). This oleylammonium iodide precursor solution remained stable and no precipitate was seen at room temperature, even when it was stored in air. The same type of solution has been previously used by us to convert CsPbBr₃ to CsPbI₃ by anion exchange.¹⁸ The mechanism of reacting amines with iodine in order to prepare alkyl ammonium iodide was hypothesized in the 70s.¹⁹ Here, it was proposed that the reaction would go through an OLAM-iodine charge transfer complex, followed by a proton-iodine exchange, resulting in alkylammonium iodide, hydroiodic acid (HI) and triiodide species, mostly in



the form of HI_3 (see **appendix 10.1**).¹⁹ Finally, the *in situ* formed HI reacts with the alkylamine, resulting in the alkylammonium iodide. This last step is similar to that of the general synthesis of alkylammonium halides, where amines are reacted with hydrogen halide solutions.^{4,20} Based on the overall reaction, a 4:1 OLAM: I_2 ratio is needed to allow for a full conversion of the I_2 to I^- . Here, a slight excess of OLAM was used (OLAM: I_2 4.6:1) to promote a full conversion. Furthermore, lower amounts of OLAM resulted in the precipitation of the oleyl ammonium iodide.

Although it is difficult to confirm the formation of the various intermediates (which is beyond the scope of this work), the presence of oleylammonium iodide can be proven with both optical absorption and nuclear magnetic resonance (NMR) spectroscopy. When I_2 was dissolved in OLAM at room temperature, the solution quickly turned dark brown and featured three absorption bands which peaked at 520 nm, 360 nm, and 280 nm (see **figure 10.1b**). These are ascribed to the I_2 charge transfer complexes (520 nm) and to HI_3 (360 nm and 280 nm).^{19,21-22} When the solution was heated up to 120 °C, it quickly turned light brown (see **appendix 10.2**). The appearance of I^- (and hence the appearance of oleylammonium iodide) upon heating could be tracked by optical absorption spectroscopy, as is shown in Figure 1b. Here, the lower energy absorption bands disappeared, and a new strong absorption appeared at around 220 nm, matching that of previous reports on I^- .^{21,23} ^1H NMR spectra of the OLAM- I_2 mixture were recorded before and after heating, as is reported in **figure 10.1c** and **appendix 10.3**. Before heating, the resonances of the CH_2 in position α to the amine remained unchanged, indicating that the amine does not become protonated under these conditions; rather, it is engaged in a charge transfer complex with I_2 .²¹ After the OLAM- I_2 solution was heated to 120 °C, the α - CH_2 peaks exhibited an increase in the chemical shift of 0.22 ppm. The extent of the chemical shift is close to that of the α - CH_2 peaks of OLAM in a 1:1 mixture with OA, as has been discussed in a previous work of ours, and this is ascribed to the protonation of OLAM.²⁴ Finally, it should be noted that the dialkylhydrazine byproduct quickly decomposes due to its high instability when it is reacted with air or OA and therefore is expected not to have an influence on the nanocrystal synthesis.¹⁹

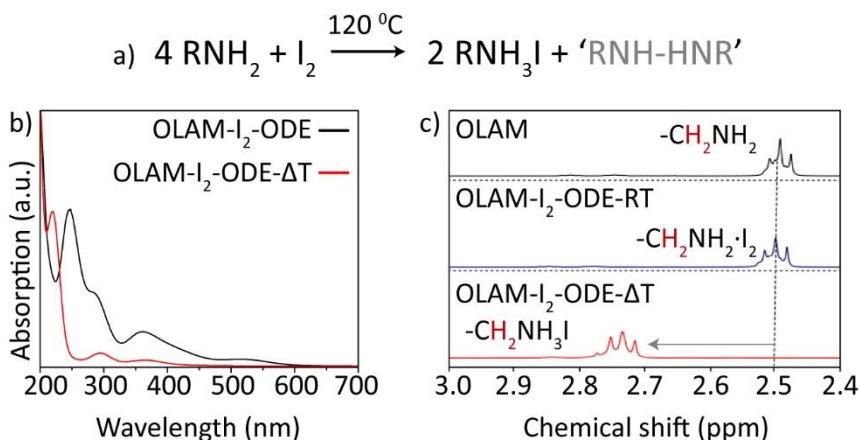
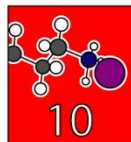


Figure 10.1. The formation of the oleylammonium precursor. (a) The proposed reaction of iodine and OLAM, leading to oleylammonium iodide (see also reaction scheme **appendix**

10.1. (b) Optical absorption spectra of the OLAM-I₂ mixture before and after heating it to 120 °C, indicating the appearance of I⁻ species after heating (absorption band at around 220 nm). **(c)** A selected region of the ¹H NMR spectra of the OLAM-I₂ before and after heating to it 120 °C. Upon heating, OLAM is protonated. The full spectra and an assignment of the resonances are reported in **appendix 10.3**

10.3 Synthesis of lead iodide perovskite nanocrystals

To explore the versatility of the *in situ* synthesized oleylammonium iodide precursor, a wide variety of metal iodide NCs were synthesized using a general synthesis, as is shown in **scheme 10.1b**. Here, the oleylammonium iodide was injected into an 80-65 °C solution containing metal oleates in OA and ODE. Upon injection, the iodide reacts with the metals, forming metal iodide NCs, and the oleylammonium and oleate react to form oleylammonium oleate (or the respective neutral molecules, OA and OLAM, at lower temperatures).²⁴ Both inorganic (CsPbI₃) and hybrid organic-inorganic (FAPbI₃) perovskite NCs were synthesized, as is reported in **figure 10.2** (see the *experimental section* for details on the synthesis). The bright red-emitting CsPbI₃ NCs were about 12 nm in size and a PL peak centered at 688 nm (1.80 eV) and a full-width at half maximum (FWHM) of 33 nm (~86 meV). The bright, near infrared emitting FAPbI₃ NCs, which were about 14 nm in size, had a PL spectrum centered at 762 nm (1.62 eV) and a FWHM of 64 nm (~138 meV). The freshly made CsPbI₃ and FAPbI₃ NC samples had high PL quantum yields (PLQY) of 79±4% (CsPbI₃ NCs, under a 510 nm excitation) and 74±3% (FAPbI₃ NCs, under a 600 nm excitation). Both the CsPbI₃ and FAPbI₃ NCs evidenced multiexponential PL decays with similar 1/e lifetimes of ~40 ns under a 508 nm pulsed excitation (see **appendix 10.4**). Therefore, these lead iodide perovskite NCs, which were prepared using off-the-shelf chemicals in air on a hotplate, had optical properties on par with the ones synthesized under an inert atmosphere with degassed precursors.²⁵ The use of oleylammonium iodide as precursor, as well as an excess of iodide during the synthesis, led to an increase in stability, as has been previously reported by others.²⁰ Both the CsPbI₃ and FAPbI₃ NCs remained colloiddally stable (redispersible) and brightly emissive for at least two weeks; the films showed little degradation, and only the FAPbI₃ NCs exhibited some minor degradation of the δ-FAPbI₃ phase (see **appendix 10.5** and **10.6**). In addition to emissive iodide perovskite NCs, wide-gap zero-dimensional Cs₄PbI₆ NCs could also be synthesized by simply increasing the Cs:Pb ratio, as is shown in **appendix 10.7**.^{10, 26}



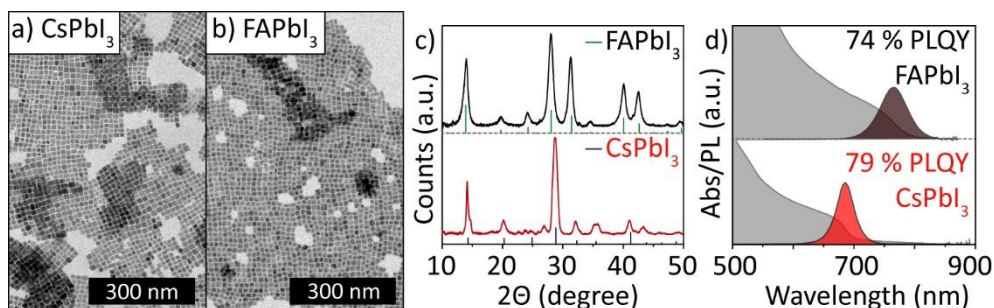


Figure 10.2. Lead iodide perovskite nanocrystals. (a-b) TEM images of CsPbI₃ and FAPbI₃ NCs, indicating narrow size distributions. (c) XRD patterns of CsPbI₃ and FAPbI₃ NCs, matching the cubic perovskite crystal structure. (d) Absorption and PL of CsPbI₃ and FAPbI₃ NCs. The XRD reference pattern of CsPbI₃ and FAPbI₃ corresponds to 98-018-1288 and 01-084-2966 respectively.

10.4 Synthesis of binary alkali-metal iodide nanocrystals

The present synthesis approach can be easily extended to other iodide-based NCs. As shown in **figures 10.3** and **appendix 10.8**, injecting the iodine precursor into an ODE solution containing an alkali metal-oleate lead to the nucleation and growth of alkali iodide NCs with a narrow size distribution. The KI and RbI NCs crystallized in a simple cubic ($Pm\bar{3}m$) crystal structure with a cubic habit, whereas the CsI NCs crystallized into in a face centered cubic ($Fm\bar{3}m$) crystal structure, with a cubo-octahedral habit. Similar to other reports on CsI NCs, all the alkali metal NCs had an absorption band at around 220-230 nm, as is shown **appendix 10.9a**.¹¹ It is interesting to note that the absorption band of these NCs is similar to that of oleylammonium iodide (see **appendix 10.9b**). These types of NCs could be interesting for use in scintillators, which is a common application for bulk CsI.

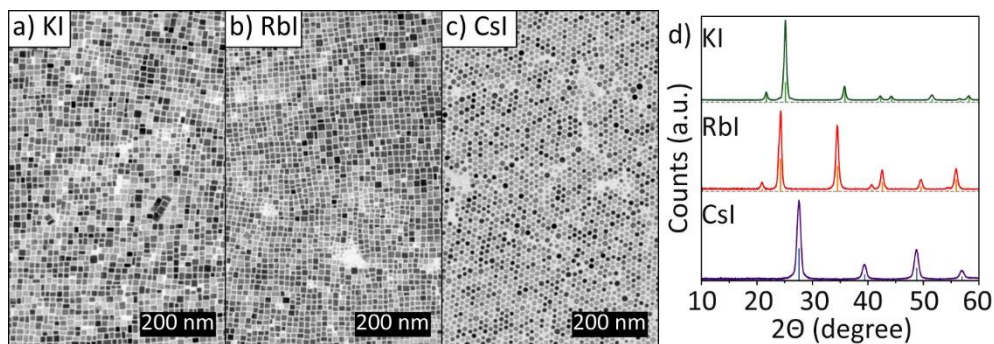


Figure 10.3. KI, RbI and CsI nanocrystals. TEM image of monodisperse (a) 14 nm KI, (b) 16 nm RbI and (c) 14 nm CsI NC. (d) XRD patterns of KI, RbI and CsI NCs, matching their respective reference patterns. XRD reference patterns of KI, Rb and CsI correspond to 96-900-8655, 96-900-8711 and 96-900-8791 respectively.

10.5 Synthesis of ternary bismuth iodide nanocrystals

The ability to introduce iodine independent from the metal precursors in the reaction flask allowed us to further extend the OLAM-I method for the synthesis of lead-free ternary bismuth iodide NCs such as Cs₃Bi₂I₉ and FA₃Bi₂I₉ NCs as shown in **figure 10.4a** and **10.4b**. While Cs₃Bi₂I₉ and MA₃Bi₂I₉ have been extensively investigated, mainly with the

aim replaced replacing lead based perovskites in photovoltaic devices,²⁷⁻²⁹ its organic formamidinium counterpart, $\text{FA}_3\text{Bi}_2\text{I}_9$, has only very recently been reported as a bulk material.³⁰ Both $\text{Cs}_3\text{Bi}_2\text{I}_9$ and $\text{FA}_3\text{Bi}_2\text{I}_9$ NCs crystallized in the Cs_3CrCl_9 crystal structure (see **figure 10.4c**),³¹ in which isolated $[\text{Bi}_2\text{I}_9]^{3-}$ clusters made of two face-sharing octahedra are surrounded by either Cs^+ or FA cations. Here, $\text{FA}_3\text{Bi}_2\text{I}_9$ is characterized by a slightly larger unit cell than $\text{Cs}_3\text{Bi}_2\text{I}_9$, due to the increased ionic radius of the FA compared to that of Cs^+ .³⁰ Similar to previous reports, the $\text{Cs}_3\text{Bi}_2\text{I}_9$ and $\text{FA}_3\text{Bi}_2\text{I}_9$ NCs had a strong excitonic absorption peak at around 500 nm (see **figure 10.4d**), originating from the absorption of the single $[\text{Bi}_2\text{I}_9]^{3-}$ clusters. This absorption peak is almost identical for $\text{Cs}_3\text{Bi}_2\text{I}_9$ and $\text{FA}_3\text{Bi}_2\text{I}_9$, as the monovalent cation has very little influence on the optical transitions within the $[\text{Bi}_2\text{I}_9]^{3-}$ clusters.

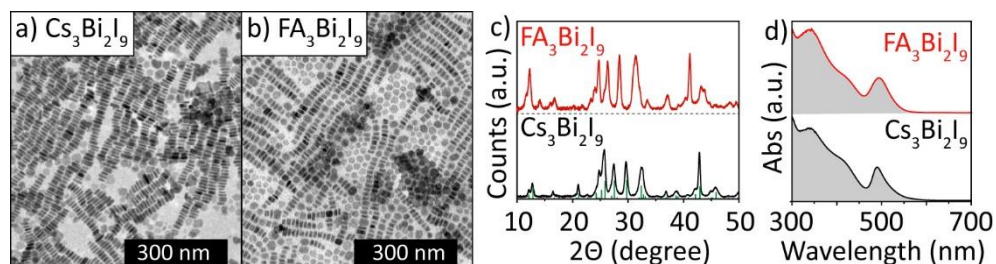


Figure 10.4. $\text{Cs}_3\text{Bi}_2\text{I}_9$ and $\text{FA}_3\text{Bi}_2\text{I}_9$ nanocrystals. TEM images of monodisperse (a) $\text{Cs}_3\text{Bi}_2\text{I}_9$ and (b) $\text{FA}_3\text{Bi}_2\text{I}_9$ platelet shaped NCs, with their respective (c) XRD patterns and (d) absorption spectra. The XRD reference pattern of $\text{Cs}_3\text{Bi}_2\text{I}_9$ corresponds to 98-000-1448.

10.6 Synthesis of binary and ternary silver-based iodide nanocrystals

Finally, the OLAM-I approach was extended to the synthesis of binary and ternary silver iodide based NCs. As is shown in **figure 10.5**, AgI NCs with a size of about 25 nm, and RbAg_4I_5 NCs of approximately 19 nm could be synthesized. RbAg_4I_5 is a superionic conductor which is characterized by a very high Ag^+ conductivity even at low temperatures, thus it is used as a solid electrolyte.³²⁻³⁴ This makes RbAg_4I_5 a promising material for all-solid-state super capacitors.³⁵ The crystal structure of the RbAg_4I_5 NCs matches that of previously reported RbAg_4I_5 .³³

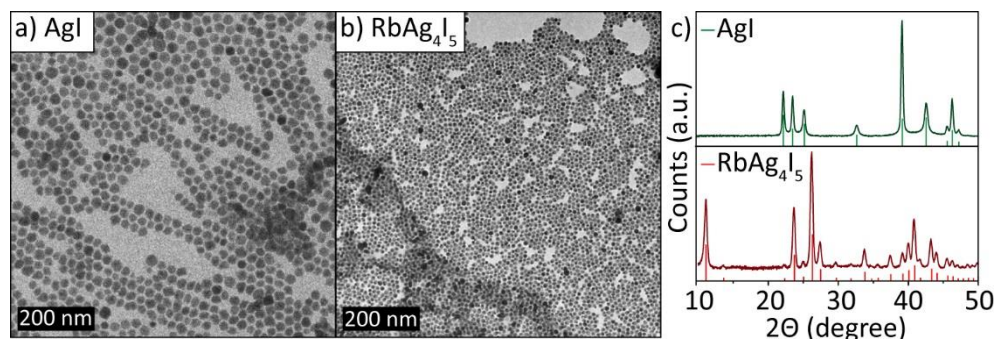


Figure 10.5. AgI and RbAg_4I_5 nanocrystals. TEM images of monodisperse (a) AgI and (b) RbAg_4I_5 NCs. (c) XRD patterns of AgI and RbAg_4I_5 NCs, matching with their respective reference patterns (96-101-1026 and 96-150-9880)



10.7 Conclusions

This chapter presented a fast and tunable synthesis method for a wide variety of metal iodide NCs. This protocol allows us to access high quality LHP NCs with PLQYs above 70%, and it can also be used to screen new metal iodide based NCs such as the reported KI, RbI, FA₃Bi₂I₉ and RbAg₄I₅ NCs. The simplicity of this hot plate based synthesis in air, combined with the use of an air stable iodide precursor at room temperature, renders this method suitable for high-throughput syntheses of NCs; synthesis robots or droplet-based microfluidic reactors, for instance, could be used.³⁶⁻³⁷

10.8 Acknowledgements

The following people contributed to this chapter:

Luca Goldoni performed the NMR experiments on the OLAM-I precursor and **Dmitry Baranov** performed the optical characterization of the perovskite NCs. Finally, **Muhammad Imran** helped with the synthesis of the FAPbI₃ NCs and **Liberato Manna** provided the final supervision on all presented work.

The research leading to these results has received funding from the European Union Seventh Framework Programme under Grant Agreement No. 614897 (ERC Consolidator Grant “TRANS-NANO”) and the framework Programme for Research and Innovation Horizon 2020 (2014–2020) under the Marie Skłodowska-Curie Grant Agreement PerovSAMs No. 747599., as well as from the Spanish Ministry of Science, Innovation and Universities via the Unidad de Excelencia María de Maeztu Grants MDM-2015-0538, MAT2017-88821-R.

10.9 Experimental section

Chemicals. Iodine, (I₂, 99.8%), potassium acetate (KAc, 99%), rubidium carbonate (Rb₂CO₃, 99%), cesium carbonate (Cs₂CO₃, 99%), lead(II) acetate trihydrate (PbAc₂·3H₂O, 99.99%), formamidinium acetate (FAAc, 99%), bismuth acetate (BiAc₃, 99.99%), silver acetate (AgAc, 99.99%), octadecene (ODE, technical grade, 90%), oleylamine (OLAM, 98%), oleic acid (OA, 90%), toluene (TOL, anhydrous, 99.8%) and toluene-d₈ (d-TOL, anhydrous, 99.6 atom % D) were purchased from Sigma-Aldrich. All chemicals were used as received, without any further purification.

Oleylammonium iodide (OLAM-I) precursor synthesis. The OLAM-I precursor (0.4 M I⁻) was prepared by reacting iodine with OLAM on a hotplate, in a similar way to previous synthesis (see **appendix 10.1**).¹⁸ Here, 1.5 grams of I₂ (0.06 mol I₂) were added to a 40 ml glass vial together with 9 ml of OLAM (0.027 mol) and 21 ml of ODE. The vial was placed on a hotplate that was set to 200 °C, and the I-OLAM solution was heated up until 120 °C, at which point the solution quickly turned light brown (in just a few seconds, see **appendix 10.2**), indicating the formation of an OLAM-I complex. The OLAM-I solution was allowed to cool and was stored under ambient conditions.

General metal iodide NC synthesis and purification. The metal iodide NCs were synthesized based on a hotplate synthesis that had previously been used to prepare Cs₄PbX₆ NCs.¹⁰ In general, the precursor salts were loaded into a 20 ml glass vial together with 5 ml ODE and varying amounts of OA (see **appendix table 10.1**). The vial was placed on a hotplate that was set to 150–200 °C, and the salts were allowed to dissolve (FAAc was dissolved at temperatures that were higher than the final reaction temperature). When the salts were fully dissolved, and as the solution reached the reaction temperature, the OLAM-I precursor was injected (1–2 ml) and the solution was cooled after 10 seconds by immersing it in an ice water bath. Finally, the NCs were separated from the reaction solution by centrifugation at 6000 rpm for 5 min, followed by redispersion in 5 ml of toluene. All reactions were carried out under ambient conditions.

Transmission Electron Microscopy (TEM). Conventional TEM images were acquired on a JEOL JEM-1011 microscope equipped with a thermionic gun at an accelerating voltage of 100 kV. The samples were prepared by drop casting diluted NC suspensions onto 200 mesh carbon-coated copper grids.

Powder X-ray Diffraction (XRD) Analysis. XRD patterns were obtained using a PANalytical Empyrean X-ray diffractometer equipped with a 1.8 kW Cu K α ceramic X-ray tube and a PIXcel3D 2x2 area detector operating at 45 kV and 40 mA. The diffraction patterns were collected in air at room temperature using Parallel-Beam (PB) geometry and symmetric reflection mode. All XRD samples were prepared by drop casting a concentrated solution on a zero diffraction quartz wafer.

Optical Absorption Spectroscopy. The spectra were taken on a Varian Cary 5000 UV-vis-NIR spectrophotometer. Samples were prepared by diluting the NC solutions in toluene in quartz cuvettes with a 1 cm path length.

Photoluminescence (PL) and PL Quantum Yield (PLQY) measurements. The PL spectra were recorded with either Varian Cary Eclipse or FLS920 Edinburgh Instruments spectrofluorimeters in a 90° geometry. Samples were prepared by diluting the various NC solutions in toluene, in quartz cuvettes with a path length of 1 cm. To report the emission peak and full-width at half maximum (FWHM) in eV, the PL spectra were converted from the wavelength to energy scale by multiplying each intensity by λ^2 .³⁸ The PLQYs of FAPbI₃ and CsPbI₃ NC samples were measured on the day of their synthesis using an FLS920 Edinburgh Instruments spectrofluorimeter equipped with the integrating sphere. PLQYs of two different batches of each FAPbI₃ and CsPbI₃ NCs were measured yielding similar results. The samples for PLQY were prepared in air by diluting 15-60 microliters of the concentrated NC solutions in toluene with 3 ml of anhydrous toluene in quartz cuvettes with 1 cm path length, capped with white PTFE stoppers (Hellma-Analytix, part number 111-10-40). The measurements were completed ca. 30-60 minutes after dilution (storing very dilute solutions for longer periods of time resulted in NCs aggregation and precipitation on the walls of the cuvette), and used matching total volume of toluene in the cuvette of the same kind as the reference blank. The concentrations of diluted NC solutions had an absorbance of ~0.1-0.2 at the stated excitation wavelength, as measured in a 1 cm path length cell with a Cary 500 spectrophotometer, or ~15-30% extinction of the integrated excitation line relative to the reference blank, as calculated from the photon number spectra that were measured with the integrating sphere. The samples were excited at 600 nm (FAPbI₃ NCs) or at 510 nm (CsPbI₃ NCs) using the output of a continuous xenon lamp (Xe900) with an excitation bandwidth of 10 nm. The photon number spectra for the samples and the blanks were collected over 575-850 nm (FAPbI₃ NCs) or 485-850 nm (CsPbI₃ NCs) spectral ranges with PMT detector with a step size of 1 nm, and a dwell time of 0.2 s per step. Corrections for the background, PMT detector sensitivity, and the lamp reference detector were applied automatically during the data collection by the software. For PLQY calculations, photon number spectra were integrated in the ranges of 585-615 nm and 650-830 nm in order to determine the total number of scattered and emitted photons, respectively, for each pair of the reference blank and FAPbI₃ NC samples; the 495-525 nm and 625-775 nm integration ranges were used for each pair of the reference blank and CsPbI₃ NC samples. The PLQY values are reported as an average of six independent measurements +/- standard deviation (74+/-3% for FAPbI₃ NCs and 79+/-4% for CsPbI₃ NCs), and they represent the “observed” PLQYs (i.e. uncorrected for the self-absorption affects).

Photoluminescence lifetime measurements. Time-dependent PL intensity decays were measured shortly after the PLQY measurements on the same samples using the time-correlated single photon counting (TCSPC) technique with the same spectrofluorimeter. The samples of both the FAPbI₃ and CsPbI₃ NCs were excited with a 508 nm picosecond pulsed diode laser (EPL-510, Edinburgh Instruments). The PL decays were collected at the peak of the emission spectra (762 nm for FAPbI₃ NCs and 688 nm for CsPbI₃ NCs) with an emission slit width of 4 nm. Both decays are multi-exponential (at least two lifetimes are needed for a satisfactory fit of the FAPbI₃ NCs' PL decay, and three for CsPbI₃). Comparatively, the CsPbI₃ NC sample demonstrates a faster decay than the FAPbI₃ NC sample,



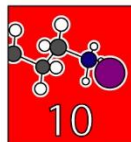
although both have similar $1/e$ decay times (~ 43 ns for the FAPbI_3 NC sample and ~ 40 ns for the CsPbI_3 NC sample).

Nuclear magnetic resonance. ^1H NMR spectra were acquired at 300.0 K on a Bruker Avance III 400 MHz spectrometer equipped with a Broad Band Inverse probe (BBI), using 4 transients and 64k data points, no steady state scans, over a spectral width of 20.55 ppm (offset at 6.175 ppm), at a fixed receiver gain (1). A line broadening of 0.3 Hz was applied to the FIDs (Free Induction Decays) before Fourier Transform. The chemical shift was referred to residual peak of not deuterated toluene at 7.09 ppm. Samples were prepared by diluting the oleylammonium iodide precursor, as well as OLAM and ODE separately, directly in d-toluene.

References

1. Protesescu, L., et al., Nanocrystals of Cesium Lead Halide Perovskites (CsPbX_3 , X = Cl, Br, and I): Novel Optoelectronic Materials Showing Bright Emission with Wide Color Gamut. *Nano Lett.* **2015**, *15*, 3692-3696.
2. Akkerman, Q. A., et al., Genesis, Challenges and Opportunities for Colloidal Lead Halide Perovskite Nanocrystals. *Nat. Mater.* **2018**, *17*, 394-405.
3. Kovalenko, M. V., et al., Properties and Potential Optoelectronic Applications of Lead Halide Perovskite Nanocrystals. *Science* **2017**, *358*, 745-750.
4. Schmidt, L. C., et al., Nontemplate Synthesis of $\text{CH}_3\text{NH}_3\text{PbBr}_3$ Perovskite Nanoparticles. *J. Am. Chem. Soc.* **2014**, *136*, 850-853.
5. Wang, A., et al., Controlled Synthesis of Lead-Free and Stable Perovskite Derivative Cs_2SnI_6 Nanocrystals Via a Facile Hot-Injection Process. *Chem. Mater.* **2016**, *28*, 8132-8140.
6. Qiu, X., et al., From Unstable CsSnI_3 to Air-Stable Cs_2SnI_6 : A Lead-Free Perovskite Solar Cell Light Absorber with Bandgap of 1.48 eV and High Absorption Coefficient. *Sol. Energy Mater. Sol. Cells* **2017**, *159*, 227-234.
7. Zhang, J., et al., High Quantum Yield Blue Emission from Lead-Free Inorganic Antimony Halide Perovskite Colloidal Quantum Dots. *ACS Nano* **2017**, *11*, 9294-9302.
8. Zhang, Y., et al., Direct-Indirect Nature of the Bandgap in Lead-Free Perovskite Nanocrystals. *J. Phys. Chem. Lett.* **2017**, *8*, 3173-3177.
9. Sun, J., et al., Lead-Free Perovskite Nanocrystals for Light-Emitting Devices. *J. Phys. Chem. Lett.* **2018**, *9*, 1573-1583.
10. Akkerman, Q. A., et al., Nearly Monodisperse Insulator Cs_4PbX_6 (X = Cl, Br, I) Nanocrystals, Their Mixed Halide Compositions, and Their Transformation into CsPbX_3 Nanocrystals. *Nano Lett.* **2017**, *17*, 1924-1930.
11. Shamsi, J., et al., Colloidal CsX (X = Cl, Br, I) Nanocrystals and Their Transformation to CsPbX_3 Nanocrystals by Cation Exchange. *Chem. Mater.* **2017**, *30*, 79-83.
12. Akkerman, Q. A., et al., Fluorescent Alloy $\text{CsPb}_x\text{Mn}_{1-x}\text{I}_3$ Perovskite Nanocrystals with High Structural and Optical Stability. *ACS Energy Lett.* **2017**, *2*, 2183-2186.
13. Liu, H., et al., Mechanistic Study of Precursor Evolution in Colloidal Group II-VI Semiconductor Nanocrystal Synthesis. *J. Am. Chem. Soc.* **2007**, *129*, 305-312.
14. Hendricks, M. P., et al., A Tunable Library of Substituted Thiourea Precursors to Metal Sulfide Nanocrystals. *Science* **2015**, *348*, 1226-1230.
15. Creutz, S. E., et al., Colloidal Nanocrystals of Lead-Free Double-Perovskite (Elpasolite) Semiconductors: Synthesis and Anion Exchange to Access New Materials. *Nano Lett.* **2018**, *18*, 1118-1123.
16. Imran, M., et al., Benzoyl Halides as Alternative Precursors for the Colloidal Synthesis of Lead-Based Halide Perovskite Nanocrystals. *J Am Chem Soc* **2018**, *140*, 2656-2664.
17. Krieg, F., et al., Colloidal CsPbX_3 (X = Cl, Br, I) Nanocrystals 2.0: Zwitterionic Capping Ligands for Improved Durability and Stability. *ACS Energy Lett.* **2018**, *3*, 641-646.
18. Akkerman, Q. A., et al., Tuning the Optical Properties of Cesium Lead Halide Perovskite Nanocrystals by Anion Exchange Reactions. *J. Am. Chem. Soc.* **2015**, *137*, 10276-10281.

19. Schug, J. C.; Kogan, M. J., The Nature of Iodine-Amine Solutions. *J. Magn. Reson.* **1973**, *11*, 406-415.
20. Dutta, A., et al., Phase-Stable CsPbI₃ Nanocrystals: The Reaction Temperature Matters. *Angew. Chem. Int. Edit.* **2018**, *57*, 9083-9087.
21. Gardner, J. M., et al., Visible Light Generation of Iodine Atoms and I-I Bonds: Sensitized I⁻ Oxidation and I₃⁻ Photodissociation. *J. Am. Chem. Soc.* **2009**, *131*, 16206-16214.
22. Im, J.-H., et al., 6.5% Efficient Perovskite Quantum-Dot-Sensitized Solar Cell. *Nanoscale* **2011**, *3*, 4088-4093.
23. Wan, L.; Xu, Y., Iodine-Sensitized Oxidation of Ferrous Ions under Uv and Visible Light: The Influencing Factors and Reaction Mechanism. *Photochem. Photobiol. Sci.* **2013**, *12*, 2084-2088.
24. Almeida, G., et al., Role of Acid-Base Equilibria in the Size, Shape, and Phase Control of Cesium Lead Bromide Nanocrystals. *ACS Nano* **2018**, *12*, 1704-1711.
25. Protesescu, L., et al., Dismantling the "Red Wall" of Colloidal Perovskites: Highly Luminescent Formamidinium and Formamidinium-Cesium Lead Iodide Nanocrystals. *ACS Nano* **2017**, *11*, 3119-3134.
26. Akkerman, Q. A., et al., Zero-Dimensional Cesium Lead Halides: History, Properties, and Challenges. *J. Phys. Chem. Lett.* **2018**, *9*, 2326-2337.
27. Ghosh, B., et al., Limitations of Cs₃Bi₂I₉ as Lead-Free Photovoltaic Absorber Materials. *ACS Appl. Mater. Interfaces.* **2018**.
28. Yang, B., et al., Lead-Free, Air-Stable All-Inorganic Cesium Bismuth Halide Perovskite Nanocrystals. *Angew. Chem.* **2017**, *129*, 12645-12649.
29. Zhang, Z., et al., High-Quality (CH₃NH₃)₃Bi₂I₉ Film-Based Solar Cells: Pushing Efficiency up to 1.64%. *J. Phys. Chem. Lett.* **2017**, *8*, 4300-4307.
30. Shin, S. S., et al., Solvent-Engineering Method to Deposit Compact Bismuth-Based Thin Films: Mechanism and Application to Photovoltaics. *Chem. Mater.* **2018**, *30*, 336-343.
31. Wessel, G. J.; Ijdo, D. J. W., The Crystal Structure of Cs₃Cr₂Cl₉. *Acta Crystallogr.* **1957**, *10*, 466-468.
32. Owens, B. B.; Argue, G. R., High-Conductivity Solid Electrolytes: MAg₄I₅. *Science* **1967**, *157*, 308-310.
33. Geller, S., Crystal Structure of the Solid Electrolyte, RbAg₄I₅. *Science* **1967**, *157*, 310-312.
34. Hull, S., et al., Crystal Structures and Ionic Conductivities of Ternary Derivatives of the Silver and Copper Monohalides: I. Superionic Phases of Stoichiometry MA₄I₅:RbAg₄I₅, KAg₄I₅, and KCu₄I₅. *J. Solid State Chem.* **2002**, *165*, 363-371.
35. Chen, C.-C., et al., Synergistic, Ultrafast Mass Storage and Removal in Artificial Mixed Conductors. *Nature* **2016**, *536*, 159-164.
36. Chan, E. M., et al., Reproducible, High-Throughput Synthesis of Colloidal Nanocrystals for Optimization in Multidimensional Parameter Space. *Nano Lett.* **2010**, *10*, 1874-1885.
37. Lignos, I., et al., Synthesis of Cesium Lead Halide Perovskite Nanocrystals in a Droplet-Based Microfluidic Platform: Fast Parametric Space Mapping. *Nano Lett.* **2016**, *16*, 1869-1877.
38. Lakowicz, J. R., *Principles of Fluorescence Spectroscopy*. 3rd ed ed.; 2009.

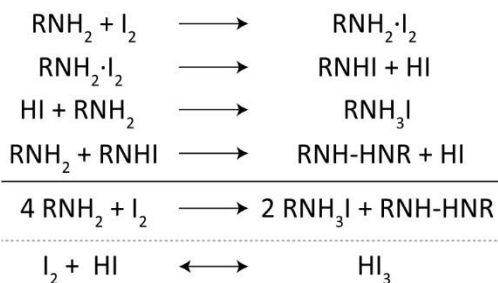


Appendices

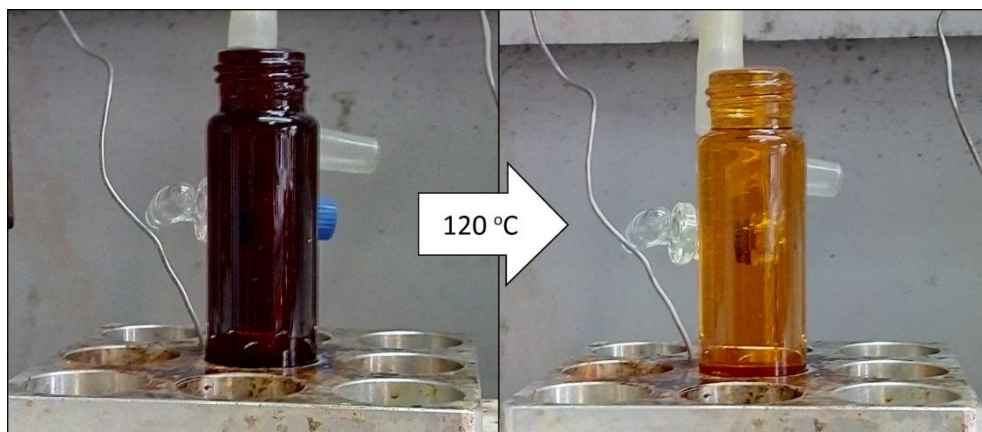
Appendix table 10.1: Reaction conditions for the synthesis of metal iodide nanocrystals

Binary					
Material	Metal precursors	OLAM-I	OA (ml)	reaction temperature	size (nm)
KI	0.2 mmol KAc	1 ml, 0.4 mmol I-	0.25	120 °C	14 ± 2
RbI	0.1 mmol Rb ₂ CO ₃	1 ml, 0.4 mmol I-	0.3	140 °C	13 ± 2
CsI	0.1 mmol Cs ₂ CO ₃	1 ml, 0.4 mmol I-	1	120 °C	14 ± 1
AgI	0.2 mmol AgAc	0.6 ml, 0.24 mmol I-	0.5	155 °C	25 ± 3
Ternary					
Material	Metal precursors	OLAM-I	OA (ml)	reaction temperature	size (nm)
CsPbI ₃	0.05 mmol Cs ₂ CO ₃ , 0.2 mmol PbAc ₂ ·3H ₂ O	2 ml, 0.8 mmol I-	0.2	165 °C	12 ± 1
FAPbI ₃	0.6 mmol FAAC, 0.2 mmol PbAc ₂ ·3H ₂ O,	1.5 mL, 0.6	3	80 °C *	14 ± 2
Cs ₄ PbI ₆	0.1 mmol Cs ₂ CO ₃ , 0.1 mmol PbAc ₂ ·3H ₂ O	2 ml, 0.8 mmol I-	0.3	100 °C	15 ± 1
Cs ₃ Bi ₂ I ₉	0.05 mmol Cs ₂ CO ₃ , 0.1 mmol BiAc ₃	1 ml, 0.4 mmol I-	1	120 °C	8.0 ± 1 x 23 ± 3
FA ₃ Bi ₂ I ₉	0.3 mmol FAAC, 0.05 mmol BiAc ₃	1 ml, 0.4 mmol I-	1	95 °C *	11 ± 1 x 18 ± 2
RbAg ₄ I ₅	0.025 mmol Rb ₂ CO ₃ 0.2 mmol AgAc	0.6 ml, 0.24 mmol I-	0.5	155 °C	19 ± 2

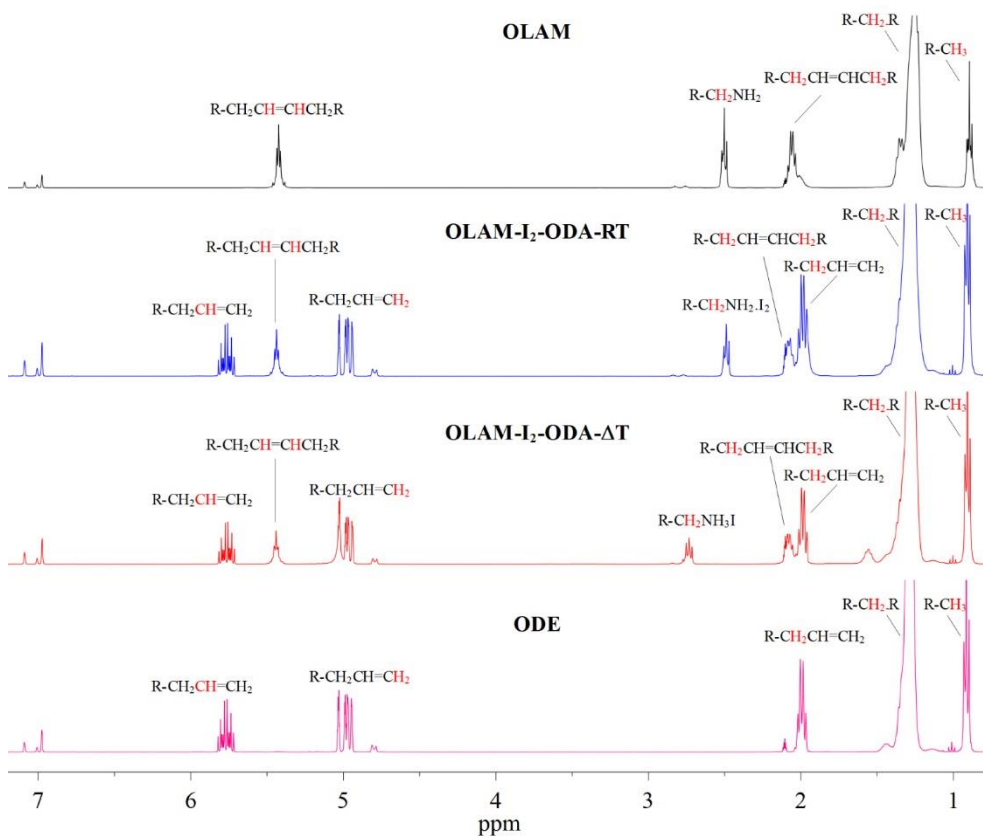
* FAAC based syntheses were first heated to 120 °C in order to dissolve the FAAC. After the FAAC had been fully dissolved, the temperature was lowered to the required temperature



Appendix 10.1. Literature proposed reaction of an amine reaction with iodine, thus forming ammonium iodide.¹

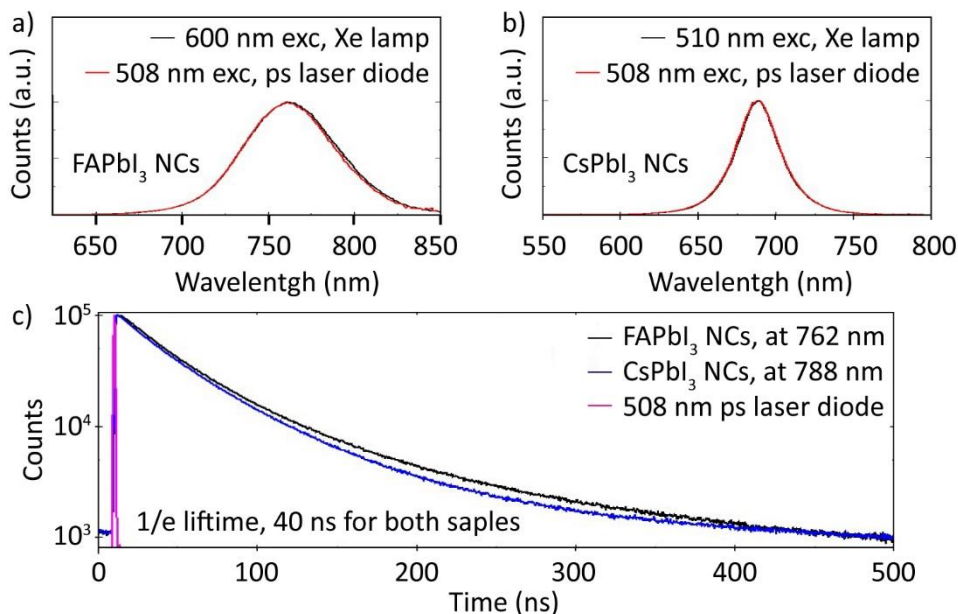


Appendix 10.2. A photo of the vial containing the OLAM-I precursor before and after the reaction at 120 °C.

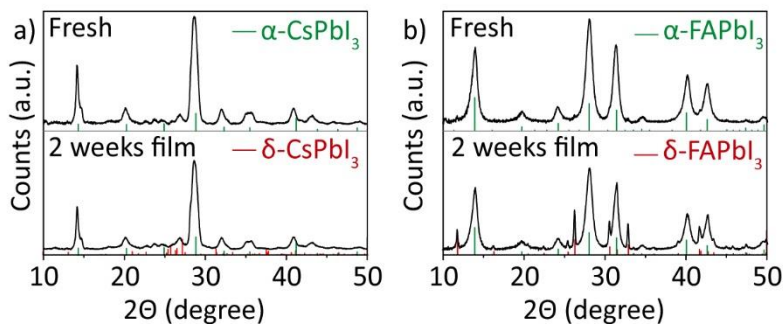


Appendix 10.3. Superimposed ^1H NMR spectra of ODE, OLAM and the OLAM-I₂ precursor before and after the reaction at 120 °C. Resonance assignment of the isolated compound (or in mixture) is marked in red beside the corresponding ^1H NMR signal. The chemical shift remained unchanged after heating for all resonances except the α - CH_2 of the OLAM.

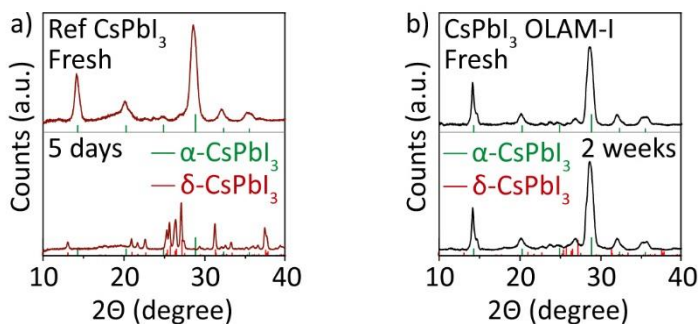




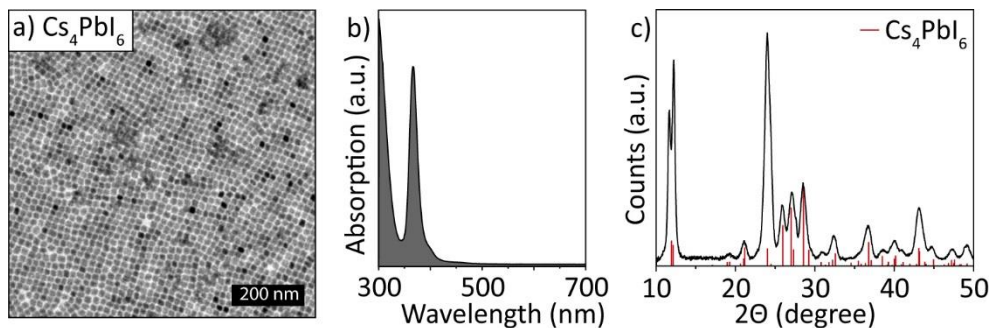
Appendix 10.4. PL data from lead iodide perovskite NCs. Emission spectra recorded under continuous excitation (for PLQY measurements) and pulsed (for lifetime measurements) excitation for (a) FAPb₃ and (b) CsPbI₃ NCs. (c) PL intensity decay curves for the toluene solutions of the CsPbI₃ and FAPbI₃ NCs.



Appendix 10.5. Lead iodide perovskite NC film stability. XRD patterns of (a) CsPbI₃ and (b) FAPbI₃ directly after deposition, and 2 weeks deposition showing no changes in the CsPbI₃ NCs, and only the conversion of a barely detectable fraction of the cubic α-FAPbI₃ or hexagonal δ-FAPbI₃ phase. The XRD reference patterns of α-CSPbI₃, δ-CSPbI₃, α-FAPbI₃ and δ-FAPbI₃ correspond to 98-018-1288, 96-433-5640, 01-084-2966 and 01-084-2966 respectively.

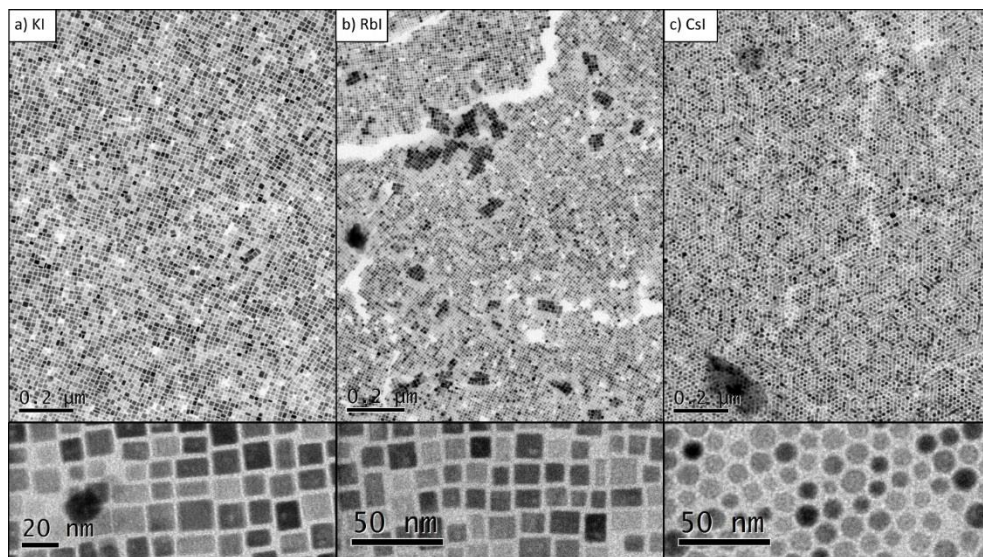


Appendix 10.6. XRD patterns of CsPbI₃ NC synthesized with the OLAM-I precursor compared to a reference CsPbI₃ sample. (a) Reference CsPbI₃ sample synthesized by injection Cs-OA into a PbI₂ solution containing OLAM, OA and ODE, showing degradation within a few days. (b) CsPbI₃ NC that were synthesized using the oleylammonium iodide injection method, showing no degradation over at least a period of two weeks. CsPbI₃ reference was adapted with permission from ref 2. Copyright 2017 American Chemical Society.

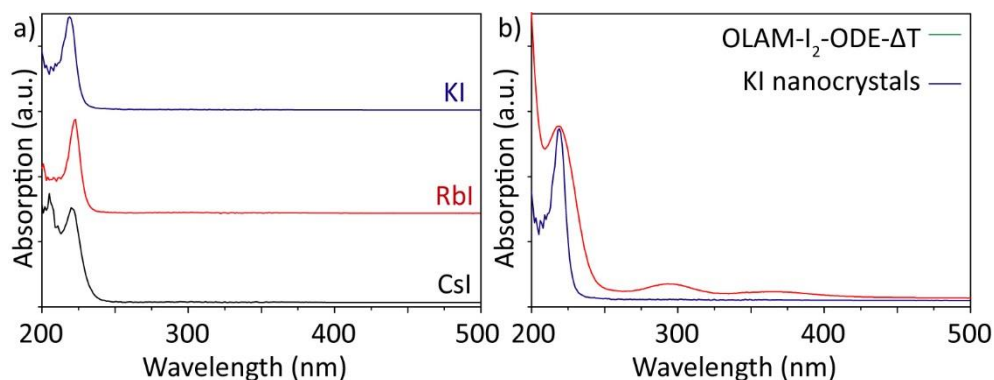


Appendix 10.7. Data on Cs₄PbI₆ NCs. a) TEM image, b) absorption spectrum and c) XRD pattern of Cs₄PbI₆ NCs. The XRD reference pattern of Cs₄PbI₆ corresponds to 04-020-2684.





Appendix 10.8. Large area TEM images of alkali metals iodide NCs. (a) KI, (b) RbI and (c) CsI NCs.



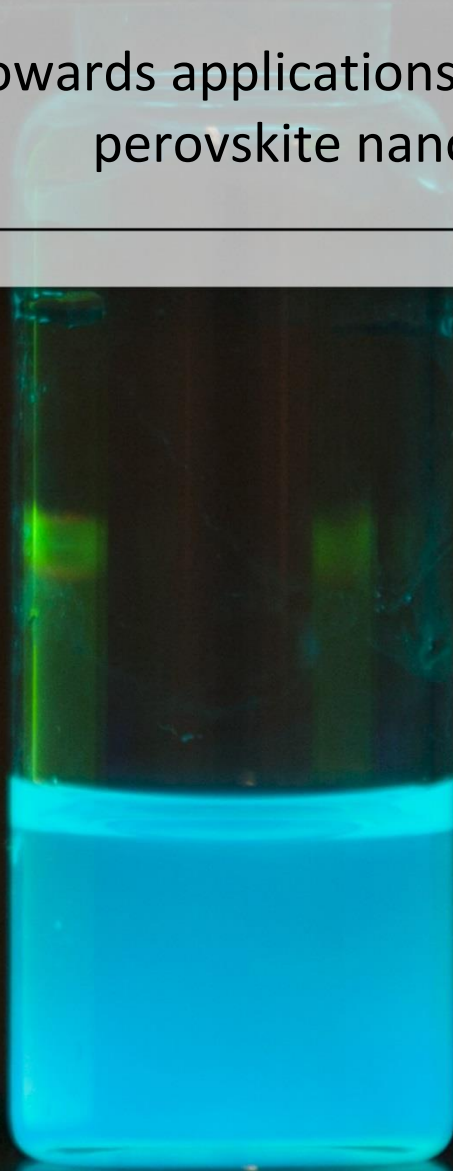
Appendix 10.9. More optical absorption spectra alkali metals iodide NCs. (a) Absorption of KI, RbI and CsI NC solutions. (b) Optical absorption spectra of KI NC solutions and of the oleylammonium precursor.

- Schug, J. C.; Kogan, M. J., The Nature of Iodine-Amine Solutions. *J. Magn. Reson.* **1973**, *11*, 406-415.
- Akkerman, Q. A., et al., Fluorescent Alloy $\text{CsPb}_x\text{Mn}_{1-x}\text{I}_3$ Perovskite Nanocrystals with High Structural and Optical Stability. *ACS Energy Lett.* **2017**, *2*, 2183-2186.



Chapter XI

Towards applications of lead halide
perovskite nanocrystals



Chapter XI: Towards applications of lead halide perovskite nanocrystals*

Abstract: *The final experimental chapter of this thesis will focus on the use of lead halide perovskite nanocrystals in optoelectronic devices. One of the main drawbacks with regard to fabricating conductive nanocrystals films is that it is difficult to preserve the nanocrystal' optical properties in solution. The majority of this chapter will focus on a fast, room-temperature synthesis of nanocrystals inks based on CsPbBr₃ perovskite nanocrystals using short ligands with a low boiling point as well as environmentally friendly solvents. These inks do not require any lengthy post-synthesis treatments, and they can be used directly to fabricate films of a high optoelectronic quality; their photoluminescence quantum yields are higher than 30%, and their amplified spontaneous emission threshold is as low as 1.5 $\mu\text{W}/\text{cm}^2$. This chapter will demonstrate that perovskite nanocrystal-based solar cells can be fabricated using these nanocrystal inks, with open circuit voltages as high as 1.5 V. This chapter will also present several lead iodide perovskite LEDs, which were fabricated based on the nanocrystals synthesized in the previous chapter.*

11.1 Introduction

Colloidal semiconductor NCs enable solution processing and represent a powerful platform for tuning optical and electrical properties useful for optoelectronic devices.¹⁻³ Over the past decades, the main challenges have been the synthesis of NC solutions with tailored properties (band gap, absorption, monodispersity) and the conversion of these solutions to high-quality NC films, with preservation of the properties.^{1-2, 4} One major problem originates directly from the synthesis methods. The high temperature (100-350 °C) syntheses often required to fabricate crystalline monodisperse and shape-controlled NCs tend to employ ligands and solvents with long alkyl chains.⁵⁻⁷ These bulky ligands and the residual chemicals from the synthesis prevent the production of dense films and form an insulating layer around the NCs after deposition onto a substrate.⁸ Strategies have been developed to overcome these issues such as the addition of conductive polymers,⁹⁻¹⁰ or post-synthesis ligand exchange.¹¹⁻¹³ Most surface passivation schemes reported so far have been based on solid-state ligand exchange, with long ligands used to stabilize the NC in solution being replaced by much shorter ligands that ensure closer NC packing and thus higher electrical conductivity.¹¹⁻¹⁴ Progress in such schemes has allowed for a steady improvement of charge-carrier diffusion lengths in solid films (above 100 nm), enabling, for example, the fabrication of thick solar-cell devices while preserving efficient charge collection, leading to record efficiencies exceeding 10%.¹⁴⁻¹⁵

Halide perovskite semiconductors can merge the highly efficient operational principles of conventional inorganic semiconductors with the low-temperature solution

*Based on *Strongly emissive perovskite nanocrystal inks for high-voltage solar cells*. **Quinten A Akkerman**, Marina Gandini, Francesco Di Stasio, Prachi Rastogi, Francisco Palazon, Giovanni Bertoni, James M Ball, Mirko Prato, Annamaria Petrozza and Liberato Manna. *Nature energy*, 2, 16194 (2016) Copyright © 2016 Springer Nature Limited.

processability of emerging organic and hybrid materials, offering a promising route towards cheaply generating electricity as well as light.¹⁶⁻¹⁹ Perovskites not only show exceptional primary optoelectronic properties such as a direct bandgap,²⁰ small exciton binding energy,²¹ low carrier recombination rates,²² ambipolar transport,²³ and tunability of the bandgap covering a wavelength range from the near-infrared²⁴ to the ultraviolet, but they are also very attractive for their ease of processability for mass production (e.g. printing from solution) and for the large availability of their chemical components. For the most efficient optoelectronic devices, the semiconductor films are currently processed from precursor solutions dissolved in organic solvents.²⁵⁻²⁸ After deposition, the constituent ions self-assemble during crystallization directly upon the selected substrate when treated at temperatures below 120 °C. Such a process can form high quality thin-films, but it also has drawbacks. Principally, it couples both the thin film morphology and the related optoelectronic properties/crystal quality in the same optimization step, making it more sensitive to processing conditions. The thin films are polycrystalline but can exhibit varying morphologies determined by different factors. These include precursor ratio, solvent, processing additives, substrate roughness and surface energy, atmospheric/environmental conditions, annealing temperature, and treatment time. As a result, the thin films contain a significant density of structural and chemical defects which introduce loss channels.

Colloidally synthesized CsPbBr₃ NCs currently can exhibit PLQYs close to 90% and can be synthesized in a wide variety of sizes and shapes.²⁹⁻³⁷ However, the enhancement in PLQY comes at the expense of carrier extraction, because the bulky organic ligands used in the synthesis of these CsPbBr₃ NCs to passivate and stabilize their surface inhibit inter-particle connectivity. This prevents their use as proper “inks” for the fabrication of dense conductive thin films.^{29-30, 36} Traditional ligand exchange procedures, as explained above, are of little help in this case, due to intrinsic lability of these NCs and the additional difficulty of purifying solutions of halide perovskite NCs from excess surfactants and unreacted precursors.³⁸⁻³⁹

In this chapter, a fast and room temperature synthesis of CsPbBr₃ perovskite NC inks using short, low boiling point ligands and solvents will be discussed (*section 11.2*). These inks have optical qualities close to those of NCs made with high temperature hot-injection syntheses. As depicted in *section 11.3*, the use of short ligands and solvents circumvents post-synthesis treatments and enables the production of thin films with high optoelectronic quality, i.e. PLQYs larger than 30% and an ASE (amplified spontaneous emission) threshold as low as 1.5 μJ/cm². Importantly, the robustness of such properties are demonstrated by the fabrication of CsPbBr₃ NCs based solar cells, with open circuit voltages as high as 1.5 V, as shown in *section 11.4*. The final two sections of this chapter will focusses on NC devices that require less complicated synthesis schemes, and were synthesized in the previous chapters; *section 11.5* will illustrate the use of lead iodide perovskite NCs used for NIR and red emitting LEDs, and *section 11.6* will present the use of CsPbCl₃ NCs alloyed with Mn²⁺ used in LSC.

11.2 Synthesis and structural characterization of CsPbBr₃ nanocrystal inks

The synthesis of the CsPbBr₃ NC inks, as depicted in **figure 11.1a**, is carried out by a simple and fast one-step injection. Propionic acid (PrAc) was used to dissolve Cs₂CO₃ and form a Cs⁺ propionate complex which is diluted in a polar/apolar solvent mixture of isopropanol (IPROH), hexane (HEX), and butylamine (BuAm) at room temperature (RT). The



dissolution reaction is exothermic and therefore does not require heating. Thus, unlike previous room temperature syntheses,³⁵⁻³⁶ no degassing was required for the precursors and the whole process was carried out under nitrogen. A separate solution, prepared under air by dissolving PbBr₂ in a similar mixture of chemicals (also at RT), was injected in the first solution. The NCs immediately nucleated and reached their maximum size already 10 seconds after the injection (see below for additional details on the growth). At this point, the NCs were separated by centrifugation and were redispersed in toluene, after which they could be directly used for device preparation. The size of the NCs could be controlled by varying the IPrOH to HEX ratio, as shown in **appendix 11.1**. Here, an increase of this ratio, and thus an increase of the polarity of the solution, led to larger crystalline domains. This route however led to unstable colloidal solutions and was thus not investigated further. As the synthesis was performed under a nitrogen atmosphere (in the glovebox) at room temperature (RT), it could be easily up-scaled to a gram sized synthesis (900 ml, 1.9 g PbBr₂), with no noticeable changes in the NC properties (**appendix 11.2**).

Important differences between this reaction scheme and previous ones (for example the one reported by Protesescu *et al.*)³⁰ are that only RT reactions were performed here, and additionally the solvents and ligands of the current synthesis have much lower boiling points (**Table 11.1**). As will be discussed later in more detail, upon spin coating of a solution of these NCs on a substrate, all these solvents and ligands quickly evaporated at RT, ensuring a fast drying of the film and facilitating the fabrication of thick films by multiple layer depositions. Also, compared to most previous syntheses of halide perovskite NCs that involved two steps,^{29, 35} the present scheme is based on a single step. Finally, and equally important, the solvents used (IPrOH and HEX) are more environmentally friendly than the classical dimethyl formamide (DMF) used in the preparation of bulk perovskite films and therefore are more amenable to scale-up in industrial processes. Additionally, hexane and toluene could be replaced with the even less hazardous heptane (bp = 98 °C) and still prepare NCs with the same features and properties (**appendix 11.3**).

CsPbBr ₃ NC inks			Cubic CsPbBr ₃ NCs ³⁰		
	bp (°C)	mL		bp (°C)	mL
IPrOH	82	4	ODE	314	5.46
HEX	69	2			
PrAc	141	0.143	OA	360	0.55
BuAm	78	0.133	OLAM	350	0.5
	Amount (mmol)			Amount (mmol)	
PbBr ₂	0.100		PbBr ₂	0.188	

Table 11.1. Boiling points and amounts of chemicals used for preparing CsPbBr₃ nanocrystal inks. Table compares the boiling points and amounts with those of standard synthesis of cubic CsPbBr₃ NCs stabilized with long ligands.^{30, 39} With propionic acid (PrAc), isopropanol (IPrOH), hexane (HEX), butylamine (BuAm), octadecene (ODE), OA (OA) and OLAM (OLAM).

As shown in **figure 11.1a** and **c**, the NCs prepared with this method tended to cluster in large aggregates. These aggregates were not formed due to the centrifugation of the NCs in the cleaning step, since similar clusters were also observed when the solution was investigated with TEM directly after the injection of the PbBr₂ precursor (and thus before washing, **appendix 11.4**). Based on HRTEM (**figure 11.1d**), they contain crystalline NCs with domains of roughly 15-20 nm in size and atomic planes matching those of orthorhombic

CsPbBr₃ (**appendix 11.5**). The crystallinity of the NC domains and the orthorhombic crystal structure was further confirmed with X-ray diffraction (XRD) analysis,⁴⁰ as reported in **figure 11.1e**. The surface Cs:Pb:Br ratios were 0.90:1.00:3.00 according to X-ray photoelectron spectroscopy (XPS) analysis, indicating a slightly Cs deficient CsPbBr₃ composition (**appendix 6**).⁴¹ XPS was further used to determine the carbon content in drop-cast samples. In a drop-cast film of 8.5 nm cubic CsPbBr₃ NCs, synthesized with octadecene (ODE), OA (OA) and OLAM (OLAM) and washed twice at 12000 rpm (as described in previous works^{30, 42}) 88 at.% of the sample surface consisted of carbon. This percentage is comparable to that reported for colloidal NCs in general (not necessarily based on halide perovskites) and synthesized under similar conditions.⁴³ For the NCs reported here, and washed only once for 2 minutes at 1000 rpm, the carbon content significantly dropped to 22 at.%, which corresponds to a ~25 fold decrease in the ratio of carbon to the overall CsPbBr₃ inorganic component. Homogenous films (see scanning electron microscope (SEM) image, **appendix 7**) could be easily prepared by spin coating and drop-casting of the NCs inks and only required about 10 min of drying under ambient conditions, whereas the 8.5 nm cubic CsPbBr₃ NCs required multiple high speed centrifugation steps (to get rid of excess ligands) and long drying times under vacuum, as already reported.^{30, 44}



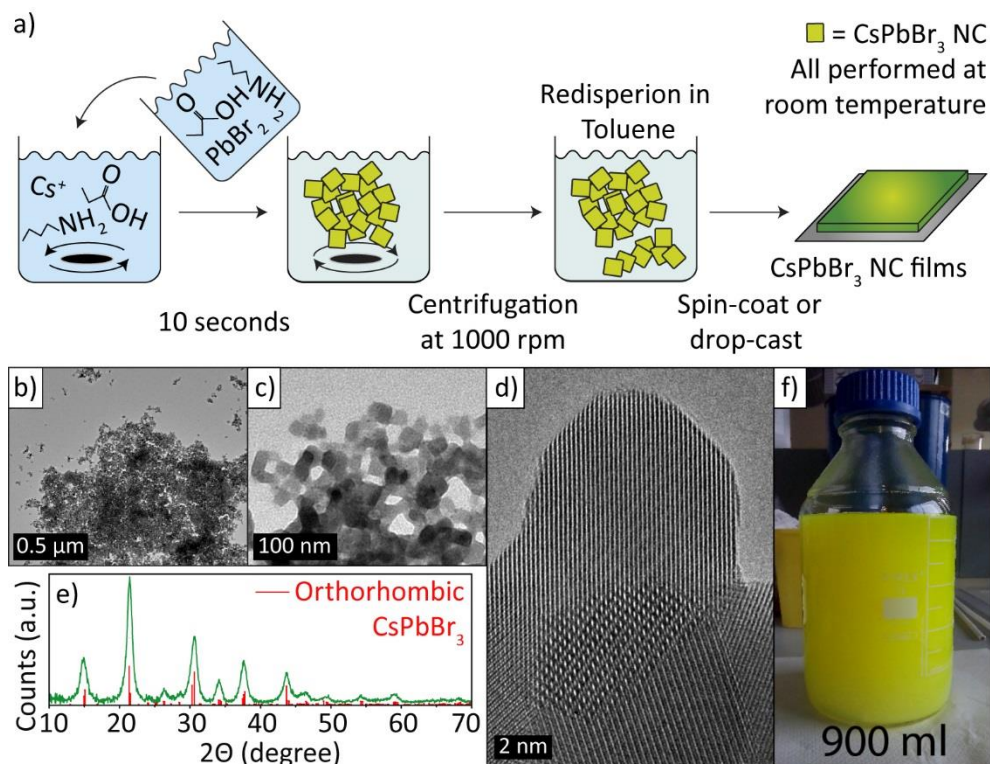


Figure 11.1. Overview of the synthesis method and structural characterization of the CsPbBr₃ nanocrystals passivated with short ligands. (a) Schematic representation of synthesis, where the PbBr₂ precursor solution is injected in a hexane/isopropanol mixture containing Cs⁺ cations. After centrifugation and redispersion in toluene, the inks can be directly used for fabrication of the films. (b-d) TEM (b, c) images and HRTEM (d) images of the CsPbBr₃ NCs. (e) XRD pattern indicating an orthorhombic crystal lattice. (f) Photo of up-scaled 2-gram synthesis. Scale bars correspond to 0.2 μm in (a), 50 nm in (b), and 5 nm in (c).

11.3 Optical characterization of CsPbBr₃ nanocrystal inks

The growth of the NCs during the synthesis was monitored over time by following their photoluminescence (PL), as shown in Supplementary Figure 8. From the data collected it is evident that the reaction takes place within the first 10 seconds from the mixing of the two solutions (see Supplementary Video 1), and that even after 2 minutes no further growth was observed. The PL and optical absorption spectra recorded on the purified CsPbBr₃ NCs, both for samples dispersed in toluene and after deposition from such dispersions to form a solid film, are shown in **figure 11.2a**. The NCs in solution had a PL peak centered at ~ 515 nm with a full-width-half-maximum (FWHM) of 24 nm, similar to that of cubic 8.5 nm NCs.^{30, 42} In the NC film, the optical absorption edge was red-shifted of about 7 nm, namely from 515 nm to 522 nm (based on the band edge), which may be attributed to a change in the local strain of the NCs in the different phase.⁴⁵⁻⁴⁶ The PL from the film consistently followed the absorption edge and retained the same Stoke shift (around 9 nm) and FWHM as in the solution. Similar PL dynamics were found in solutions and in films (**figure 11.2b**), in agreement with the fact that the PL quantum yield (PLQY) did not undergo a dramatic drop,

from about $58 \pm 6\%$ in solution to $35 \pm 4\%$ in the film (excitation density around $250 \mu\text{W}/\text{cm}^2$). Note that the PLQYs from these films were slightly higher than that typically observed from films of cubic CsPbBr_3 NCs prepared with OA and OLAM ($\approx 30\%$) which remained non-conductive.⁴²

Measurements under femtosecond (fs)-excitation were carried out to investigate the presence of amplified spontaneous emission (ASE) from the NC films, which represents a good fingerprint of their optical quality.⁴⁷ ASE was readily observed for films fabricated by spin-coating of the NCs solution onto soda-lime glass substrates (200-300 nm thick, **figure 11.2c**). The ASE peak had a FWHM between 4.3 and 4.6 nm and was red-shifted by 3 nm from the PL maximum ($\lambda_{\text{PL}} = 522 \text{ nm}$). a reduced ASE red-shift was observed compared to what reported for other CsPbBr_3 NCs,⁴⁸⁻⁵⁰ which tentatively was ascribed to the increased Stoke-shift observed the spin-coated films (9 nm, compared to other synthetic approaches,³⁶ see **figure 11.2a**), since the optical gain arises in spectral positions where the optical re-absorption is reduced (Urbach tail).⁴⁸ **figure 11.2d** reports the emission intensity vs pumping fluence, from which an ASE threshold around $2.44 \mu\text{J}/\text{cm}^2$ could be extracted. It is known that the film morphology can induce optical feedback⁵¹⁻⁵² (due to the relatively high refractive index of the NCs, $n \approx 2$, with respect to that of air) and thus modify the ASE threshold and induce random lasing. For this reason, the ASE threshold was measured from 10 different films in different positions prepared from two batches (total of 62 measurements). The threshold varied from $1.5 \mu\text{J}/\text{cm}^2$ up to $38 \mu\text{J}/\text{cm}^2$ with a median value of $9 \mu\text{J}/\text{cm}^2$. So far, $1.5 \mu\text{J}/\text{cm}^2$ is the lowest value reported for CsPbBr_3 NCs⁴⁸⁻⁵⁰ and overall for perovskite thin films (a geometry that is more suitable for the fabrication of devices such as electrically pumped lasers). This evidence supports the high optical and electronic quality of the ink and its related thin films, most likely due to a low density of electronic defects. The ASE threshold found here is actually among the lowest reported to date, even if compared to that of other inorganic NCs commonly used in laser devices (CdSe nanoplatelets,⁵³ CdSe/CdS giant-shells,⁵¹⁻⁵² and CdSe/CdS dot-in-rods.⁵⁴⁻⁵⁵



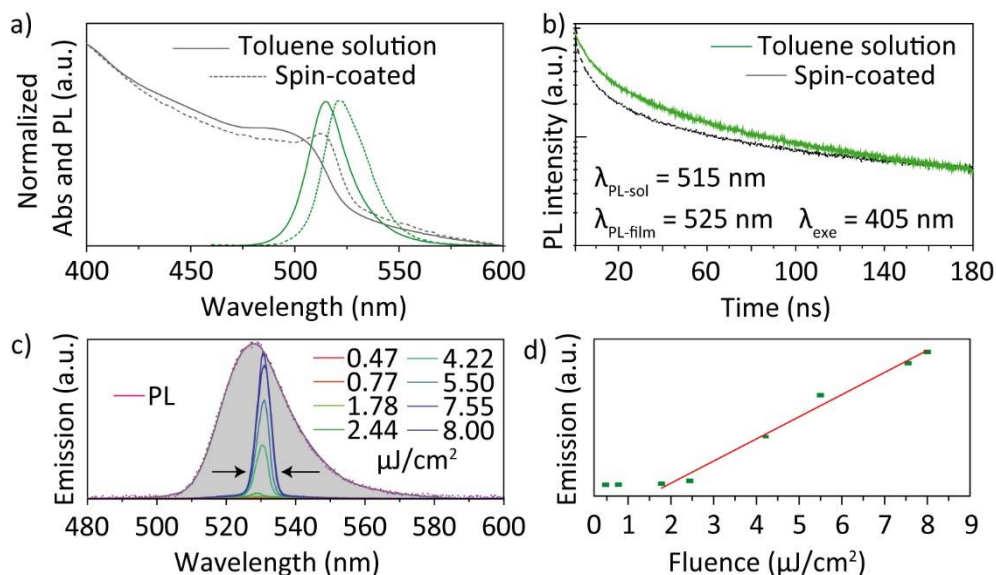


Figure 11.2. Optical characterization of CsPbBr₃ nanocrystal inks in solution and in films (a) Optical absorption and steady-state PL spectra of CsPbBr₃ NCs in toluene solution (solid line) and from a spin-coated film (dashed line). (b) Time-resolved PL measured at the PL peak for the CsPbBr₃ NCs in toluene solution (green line) and from a spin-coated film (black line). (c) Emission spectra under increasing fs-pulsed excitation fluence with ($\lambda_{\text{exc}} = 405$ nm) recorded from a spin-coated film of CsPbBr₃ NCs. An ASE peak at 531 nm is observable for pumping fluences above 2.44 $\mu\text{J}/\text{cm}^2$. (d) Emission intensity vs excitation fluence curve for the film in panel. The red line is a linear fit of the data points above threshold.

11.4 High Voltage Solar cells based on CsPbBr₃ nanocrystal inks

Wide band-gap halides perovskites such as CsPbBr₃ can achieve high open-circuit voltages and are therefore of particular interest to multi-junction solar cells, visible light-emitting devices, and solar water splitting applications.⁵⁶⁻⁵⁸ Moreover, the replacement of the organic component (methylammonium and/or formamidinium - FA) in the lead halide framework with an inorganic cation such as cesium is sought as the most promising avenue for improving the thermal compositional stability,⁵⁹⁻⁶⁰ which is important for solar cell operation. However, due to the relative insolubility of the CsBr precursor, it is difficult to achieve a high-level of control over the thin-film morphology and optoelectronic properties using conventional approaches and retain low processing temperatures. Thus, thin-film devices based on CsPbBr₃ have remained relatively unexplored to date. For testing the NCs inks reported here in solar cell devices, a state of the art architecture was used, i.e. a stack comprised of FTO-coated glass, a compact layer of titanium dioxide (c-TiO₂) as the electron-extracting layer, a layer of 2,2',7,7'-Tetrakis-(N,N-p dimethoxyphenylamino)-9,9'-spirobifluorene (Spiro-MeOTAD) as the hole-transporting material and evaporated Au as the top contact. In **figure 11.3a** a sketch reports the device stack and **figure 11.3b** reports the energy levels of each layer. For the electrodes and the charge extracting layers, values reported in the literature were used,⁶¹ while for the NC thin films the energies of the conduction and valence band edges have been extracted by adding the optical bandgap to

the position of the valence band maximum as determined by ultraviolet photoelectron spectroscopy (UPS) measurements (see *experimental section 11.6* and **appendix 11.9**).

With a single spin-coating step of the suspended CsPbBr₃ ink on the c-TiO₂ substrate, a complete coverage of the substrate was obtained. The solar cell, in this case, exhibited short circuit values (J_{sc}) of 1.26 mA cm⁻², open circuit voltage (V_{oc}) of 0.87 V, and fill factor (FF) of 0.65, leading to a power conversion efficiency (PCE) of 0.72% (see **appendix 11.10**). The reported FF and V_{oc} suggest a good electronic quality for such an extremely thin layer of perovskite, however the photocurrent was low as the film was very thin (its optical density was ~0.3, see **appendix 11.11**). A thicker film could be prepared by performing sequential deposition cycles of the NC ink. This process, which was uniquely facilitated by the low boiling point of the ligands and solvents, enabled a fast drying of the film after each deposition step, with no need to anneal the film. In particular, the fact that the perovskite from an apolar solvent could be deposited means that the active layer is resistant to subsequent NC ink deposition cycles and other spin coating steps.¹⁴⁻¹⁵

By increasing the film thickness through sequential depositions, the optical density of the sample grew monotonically (see **appendix 11.11**) while the NCs maintained their structural properties, as proven by comparing the XRD pattern of these films to the one obtained from a film deposited by simple drop casting (**appendix 11.12**). As reported in **figure 11.2c**, increasing the number of NCs deposition cycles led to a direct increase of both J_{sc} and V_{oc} of the devices, while the FF remained almost constant (**appendix 11.13** and **11.14**). An active layer with a thickness of 550 ± 50 nm (**appendix 11.15**), prepared by 9 sequential depositions, exhibited a PCE of 5.4 %, which is comparable to the best performing and fully optimized devices reported so far.^{43, 53, 55} The solar cell had J_{sc} and V_{oc} of 5.6 mA cm⁻² and 1.5 V. The value for V_{oc} is among the highest reported for perovskite halides, underlining the high quality of the active layer (for reference, the calculated maximum V_{oc} and J_{sc} are 2.05 V and 7.78 mA cm⁻² under AM1.5 illumination⁶² considering a band-gap of about 2.38 eV⁶³). The use of TiO₂ as the electron extracting layer in a flat junction architecture generally presents J-V characteristics that depend on the polarization history of the device, with a reduction of the photocurrent over time under polarization.^{62, 63} Interestingly, these devices show a rapid response of the photo-current under polarization, resulting in electrically stable steady-state power output (**appendix 11.13** and **11.14**). Finally, it is worth mentioning that, although there are several factors that determine the V_{oc} and their relative contribution is still a completely open issue in perovskite solar cells, preliminary literature reports seem to suggest that further improvements will be possible by carefully designing the charge extracting layers⁶⁴, thus highlighting the strong potential of this approach.



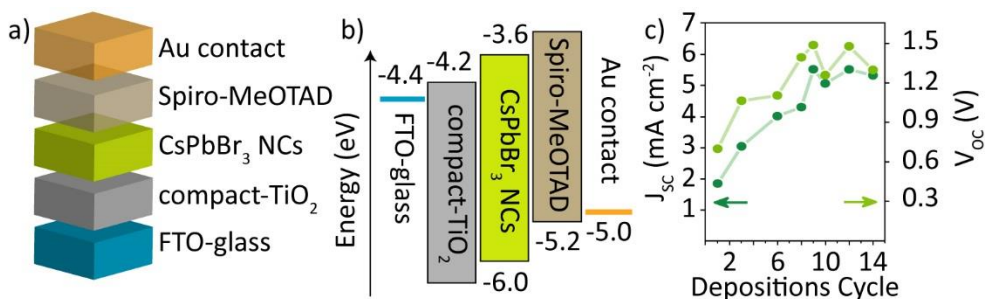


Fig. 11.3 CsPbBr₃ nanocrystal high voltage solar cells (a) Scheme of the standard architecture of the solar cell (FTO/c-TiO₂/CsPbBr₃/spiro-MeOTAD/Au). (b) Energy-level diagram of the materials used. The upper and lower edges of the boxes represent the conduction band minimum and valence band maximum, respectively. The values are stated with respect to vacuum. (c) Short circuit current (dark green dots) and open circuit voltage (light green dots) evolution for photovoltaic devices measured under AM 1.5G white light illumination, depending on the number of NC deposition cycles.

11.5 Red and emitting LEDs with lead iodide perovskite nanocrystals[†]

We have exploited the excellent optical properties of the iodide perovskite NCs that were prepared using this simple approach to fabricate deep-red and infrared light-emitting diodes (LEDs). To remove excess ligands and ODE (which often limit the use of NCs in devices)¹ from the solution, a simple “rinsing” procedure was used (see *experimental section* 11.9 and **appendix 11.16**). After the NCs had been separated from the growth solution through centrifugation, the vial was slowly (without shaking) filled with toluene, causing any residual organics that were attached to the vial to dissolve. The toluene was then removed, and the NCs were fully redispersed in toluene. The NC samples which were to be used for LED fabrication were stored at higher concentrations (6 times) compared to normal storage. Under these conditions, the NCs were stable, as no significant loss of PL was seen after the samples were exposed to air for 2 weeks. The NC LEDs were prepared by spin-coating poly(3,4-ethylenedioxythiophene)-poly(styrenesulfonate) (PEDOT:PSS) on pre-patterned ITO/ Glass coated glass substrates, followed by a layer of spin-coated NCs. The devices were finalized by evaporating 2,4,6-Tris[3-(diphenylphosphinyl) phenyl]-1,3,5-triazine (PO-T2T) as a hole blocking layer and a Ca/Ag bi-layer metal contact (see the *experimental section* for more details on device fabrication and **figure 11.4a** for a schematic representation of the device stack and approximate energy levels). To prepare the mixed (Cs:FA)PbI₃ NC LEDs, which are reported to have the highest EQE among red/NIR NC LEDs,⁶⁵ the CsPbI₃ and FAPbI₃ NCs solutions were simply mixed prior to device fabrication. Due to an interparticle cation exchange, the mixed solution exhibited a single PL peak and absorption centered between 688 nm and 762 nm, indicating a homogeneous (Cs:FA)PbI₃ composition.^{42, 66}

The electroluminescence spectra for all three devices (see **figure 11.4b**) evidenced a single-peak emission at 688 nm for CsPbI₃, 728 nm for mixed (Cs:FA)PbI₃, and 739 nm for FAPbI₃. This corresponds to a deep-red emission for the inorganic NCs, with CIE coordinates

[†]Based on: *Molecular Iodine for a General Synthesis of Binary and Ternary Inorganic and Hybrid Organic-Inorganic Iodide Nanocrystals*. **Quinten A. Akkerman**, Laura Martínez-Sarti, Luca Goldoni, Muhammad Imran, Dmitry Baranov, Henk J. Bolink, Francisco Palazon and Liberato Manna. *Chemistry of Materials*, 30, 6915–6921 (2018). Copyright © 2018 American Chemical Society

(0.6489, 0.2856), thus they are promising for wide-gamut displays and lighting. **Figure 11.4c** reports the current-voltage-radiant flux curves of the three devices. The highest radiant flux was obtained for purely inorganic CsPbI₃ NCs, exceeding 10⁶ μW/m² at 8 V. This corresponds to a luminance higher than 10,5 cd/m² - a value higher than that which has been recently reported for a similar system.⁶⁶ However, the most efficient devices were obtained using mixed (Cs:FA)PbI₃, which had an external quantum efficiency (EQE) exceeding 2% across the whole range from 2,5 V to 7 V, and a maximum EQE over 3% at around 4,3 V. These results are on par with the record EQEs that have recently been reported for NCs with a similar chemical composition.⁶⁵⁻⁶⁶ Contrary to the other two devices, the one based on pure FAPbI₃ evidenced a strong degradation of the radiance above 4V (see **figure 11.4c**), which ultimately led to a lower EQE (see **figure 11.4d**). Interestingly, the incorporation of the inorganic cation Cs⁺ to the mixed NCs resulted in an increase in the EQE of over one order of magnitude (see **figure 11.4d**), while a maximum emission close to that of pure FAPbI₃ was still maintained (see **figure 11.3b**).

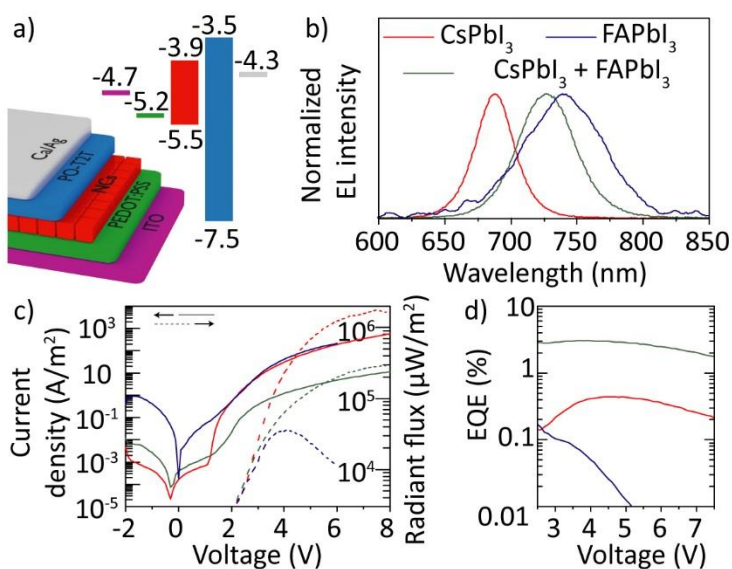


Figure 11.4 Red and NIR lead iodide nanocrystal LED device characteristics. **(a)** Schematic representation and flat band energy diagram of the LEDs that were used in this work (the energy levels of the emitting material layer in the scheme correspond to FAPbI₃). **(b)** Normalized electroluminescent spectra in which the red, blue and green curves refer to CsPbI₃, FAPbI₃ and mixed Cs/FAPbI₃, respectively. **(c)** Current-voltage-luminance and **(d)** EQE vs voltage characteristics of the NC LEDs.

11.6 Conclusion

This chapter presented the use of LHP NCs in solar cells and LEDs. Through the synthesis of CsPbBr₃ NCs which are passivated with shorter ligands than those that have been used in previously reported syntheses, NC films with a low carbon content were fabricated. The resulting films had high PLQYs (35%), and no severe degradation of the charge-carrier conduction occurred. Simple spin-coated films of these inks exhibited a record low ASE threshold of 1.5 μJ/cm². The CsPbBr₃ perovskite inks were then used to



fabricate a halide perovskite NC-based photovoltaic prototype device. Using this method, fully air-processed, electrically stable, solar cell was produced exhibiting power-conversion efficiencies exceeding 5% and an open circuit voltage higher than 1.5 V. These values are among the highest that have been achieved for perovskite-halides with a wide band-gap, and for Cs-based solar cells in general. This chapter also showed that the high external quantum yield and narrow emission spectra of red emissive CsPbI₃ and NIR emissive FAPbI₃ NCs can be used for the fabrication of LEDs of a high optical and electronic quality, without any significant washing procedures. Furthermore, it was shown that the use of mixed NCs significantly improves the LED performance. These results represent the first step towards the use of LHP NCs in actual NC-based devices.

11.7 Acknowledgments

The following people contributed to this chapter:

Marina Gandini, **James M. Ball** and **Annamaria Petrozza** fabricated, tested and studied the solar cells as presented in *section 11.4*. **Francesco Di Stasio** studied the optical properties of the films and performed the ASE measurements depicted in *section 11.3*. **Prachi Rastogi** performed the cross-section STEM and **Francisco Palazon** performed the XPS measurements on the CsPbBr₃ NC inks. **Giovanni Bertoni** performed the HRTEM measurements and **Mirko Prato** performed the UPS measurements described in *section 11.2*. **Laura Martínez-Sarti**, **Henk J. Bolink** and **Francisco Palazon** fabricated and characterized the LHP LEDs which were shown in *section 11.5*. **Liberato Manna** provided the final supervision on all presented work.

The research leading to these results has received funding from the European Union 7th Framework Programme under Grant Agreement No. 614897 (ERC Consolidator Grant “TRANS-NANO”) and from the Cariplo Foundation through grant agreement n. 2013-0656 (“Green nanomaterials for next-generation photovoltaics, GREENS”), as well as from the the Innovation Horizon 2020 (2014–2020) grant under the Marie Skłodowska-Curie Grant Agreement PerovSAMS No. 747599 and from the Spanish Ministry of Science, Innovation and Universities via the Unidad de Excelencia María de Maeztu Grants MDM-2015-0538, MAT2017-88821-R.

11.8 Experimental section

Chemicals. Lead(II) bromide (PbBr₂, 99.999% trace metals basis), cesium carbonate (Cs₂CO₃, reagentPlus, 99%), butylamine (BuAm, 99.5%) 2-propanol (iPrOH, anhydrous, 99.5%), propionic acid (PrAc, ≥99.5%), n-hexane (HEX 99.5%), titanium(IV) isopropoxide (99.999%), 4-tert-butylpyridine, and lithium bis(trifluoromethylsulfonyl)imide (LiTFSI) were purchased from Sigma-Aldrich. Toluene (TOL, anhydrous, 99.8%) was purchased from Carlo Erba reagents. 2,2',7,7'-tetrakis(N,N-di-p-methoxyphenylamine)-9,9-spirobifluorene (spiro-MeOTAD) was purchased from Lumtec. All chemicals were used without any further purification.

Synthesis and purification of CsPbBr₃ NC inks for solar cells. The synthesis is an adaptation of the synthesis for CsPbBr₃ nanoplatelets as reported previous works.³⁵ Here, 2 mL HEX, 1 mL iPrOH, and 5 μL ml Cs-PrAc (3.6M Cs⁺, Cs₂CO₃ dissolved in pure PrAc at room temperature) were mixed in air and at room temperature, forming a clear solution. Swiftly, 100 μL PbBr₂ precursor (0.5 M in 1:1:1 PrAc:iPrOH:BuAm) was injected. The solution immediately turned green and it then turned turbid within seconds. The CsPbBr₃ NCs were centrifuged for 2 min at 1000 rpm and were then redispersed in toluene.

Synthesis and purification of perovskite NCs for LEDs. The perovskite NCs for LED fabrication were synthesized as discussed in *chapter 9*, with the following exceptions: the synthesis

was upscaled; the washing procedure was adjusted; and the samples were stored more concentrated compared to normal sample storage. The synthesis was performed using three times the amount of precursors and solvents, which was finally stored in 2.5 ml of TOL, leading to approximately a 6-fold increase in the concentration compared to that of the normal synthesis. The NCs were washed using a simple 'rinsing' procedure, as is shown in **appendix 11.17**. Here, residual ligands and any ODE that adhered to the glass walls of the reaction vials after centrifugation were dissolved in TOL, without dispersing the precipitated NCs.

Solar cell fabrication. FTO-coated glass sheets were etched with zinc powder and HCl (2 M) to obtain the required electrode pattern. The substrates were sonicated in sequence with detergent (Alconox), distilled water, 2-propanol, acetone and 2-propanol again for 10 min, respectively. The substrates were then blown dry with N₂ and finally treated with oxygen plasma for 10 minutes to remove the last traces of organic residues. The TiO₂ precursor solution was prepared by mixing 6 μL of 2M HCl in 1 mL of 2-propanol to a titanium isopropoxide solution in 2-propanol (140 μL titanium isopropoxide in 1 mL of 2-propanol). This solution was then spin-coated at 2000 rpm for 60 s and then sintered at 500°C following Ball *et al.*⁶⁷ The CsPbBr₃ suspension solution was spin coated at 1000 rpm for 45 s. In order to increase the active layer thickness with subsequent deposition cycles the samples were left drying for 5 minutes at room temperature between each spinning. The samples were then transferred into a N₂-filled glove box for the deposition of spiro-MeOTAD as the hole transporting material (HTM). The HTM was spin-coated at 1000 rpm for 60 s. The solution was prepared by dissolving 75 mg of spiro-MeOTAD, 32 μL 4-tert-butylpyridine, 18.8 μL of a stock solution of 520 mg mL⁻¹ Li-TFSI in acetonitrile in 1 mL anhydrous chlorobenzene. After 12 h of exposure to dry air, a 75 nm thick gold film was thermally evaporated through a shadow mask to prepare devices with total area of ca. 0.0935 cm².

Light-emitting diode (LED) fabrication and characterization. The fabrication and characterization of the devices were carried out inside a cleanroom ISO 7 10000. Pre-patterned ITO covered glass substrates were cleaned by sonication in water with soap, deionized water and 2-propanol baths. After drying with a N₂ flow, the substrates were placed in a UV Ozone cleaner (Jelight 42-220) for 20 min. LEDs with a p-i-n configuration (p-type layer deposited on the transparent substrate) were prepared by spin-coating PEDOT:PSS (Poly(3,4-ethylenedioxythiophene)-poly(styrenesulfonate)) (Clevios P VP Al 4083) on the prepatterned ITO/glass substrates for 60 seconds at 1000 rpm, which were then thermally annealed for 15 min at 150 °C. The NC dispersions (either the CsPbI₃, FAPbI₃, or Cs/FAPbI₃ NCs) were drop cast on top of the PEDOT:PSS layers and left for 2 minutes to slowly evaporate prior to being spin-coated for 60 seconds at 1500 rpm. The devices were then transferred to an inert atmosphere glovebox (<0.1 ppm O₂ and H₂O), where they were finished by a vacuum deposition of a 45 nm layer of 2,4,6-Tris[3-(diphenylphosphinyl)phenyl]-1,3,5-triazine (PO-T2T), acting as an electron transport/hole blocking layer, and a Ca/Ag (7/100 nm) bi-layer metal contact. The LEDs were characterized under inert conditions inside the glovebox at room temperature. The active area of the devices was 4 mm². The current density and the electroluminescence versus voltage characteristics were measured using a Keithley 2400 Source-Meter and an integrated sphere coupled to a UDT instruments S370 Optometer. An Avantes AvaSpec-2048 Fiber Optic Spectrometer was used to measure the electroluminescent spectra.

Transmission Electron Microscopy. Conventional transmission electron microscopy (TEM) images were acquired on a JEOL JEM-1011 microscope equipped with a thermionic gun at 100 kV accelerating voltage. High-resolution TEM (HRTEM) imaging was performed on a JEOL JEM-2200FS microscope equipped with a Schottky gun operated at 80-200 kV accelerating voltage, a CEOS spherical aberration corrector in objective lens enabling a spatial resolution of 0.9 Å, and an in column Ω-filter. The samples were prepared by drop casting diluted NPLs colloidal suspensions onto 200 mesh carbon-coated copper grids for conventional TEM imaging, and 400 mesh ultrathin carbon-coated copper grids for HRTEM imaging, respectively. To avoid or reduce the diffusion of Pb induced by the electron beam, the images were taken by summing multiple fast acquisitions (≤0.2 sec) after drift correction, by using a K2 direct detection camera (Gatan, Inc.), allowing low doses (<5e⁻/pixel-sec).



X-ray and ultraviolet photoelectron spectroscopy . These analyses were performed on spin-cast films of CsPbBr₃ NC inks, respectively, to evaluate the chemical composition and to estimate the position of the valence band maximum (VBM) of the materials under investigation. The measurements were carried out with a Kratos Axis Ultra^{DL} spectrometer. For XPS measurements, high resolution spectra of Cs 3d, Pb 4f, Br 3d and C 1s peaks were acquired at pass energy of 10 eV using a monochromatic Al K α source (15 kV, 20 mA). The UPS measurements were performed using a He I (21.22 eV) discharge lamp, on an area of 55 μ m in diameter, at pass energy of 5 eV and with a dwell time of 100 ms. The work function (i.e. the position of the Fermi level with respect to vacuum level) was measured from the threshold energy for the emission of secondary electrons during He I excitation. A -9.0 V bias was applied to the sample in order to precisely determine the low kinetic energy cut-off, as discussed by Helander *et al.*⁶⁸ Then, the position of the VBM vs vacuum level was estimated by measuring its distance from the Fermi level.⁶⁹⁻⁷⁰

Optical Absorption Spectroscopy. The spectra were taken on a Varian Cary 5000 UV-vis-NIR spectrophotometer. Samples were prepared by diluting the NC solutions in toluene (20 μ L in 1 mL) in 1 cm path length quartz cuvettes. Samples of thin films were prepared by spin-coating the NCs on a c-TiO₂/FTO substrate or a soda-lime glass substrate.

PL and PL quantum yield measurements. PL measurements were carried out on solutions and films with an Edinburgh Instruments fluorescence spectrometer (FLS920), which included a Xenon lamp with monochromator for steady-state PL excitation, a calibrated integrating sphere for PL quantum yield (PLQY) measurements and a time-correlated single photon counting unit coupled with a pulsed laser diode (λ = 405 nm, pulse width = 50 ps) for time-resolved PL studies. Solutions were prepared in quartz cuvettes and carefully diluted to 0.1 optical density at the excitation wavelength (λ = 400 nm) while films were prepared via spin-coating in air on soda-lime glass substrates. PLQY measurements on films were carried out using the procedure developed by J. C. De Mello *et al.*⁷¹

Amplified Spontaneous Emission measurements. Films of CsPbBr₃ NCs spin-coated on soda-lime glass were excited with λ = 405 nm using an amplified Ti:sapphire laser (Coherent Legend Elite seeded by a Ti:sapphire fs laser) with a 70 fs pulse (FWHM) and a repetition rate of 1 kHz. The ASE measurements were performed by focusing the excitation beam with a cylindrical lens onto the sample, thus obtaining a stripe shaped beam profile. All ASE spectra were collected at \sim 90° with respect to the excitation beam with an Ocean Optics HR4000 spectrometer coupled with an optical fiber.

Powder X-ray Diffraction Analysis. XRD patterns were obtained using a PANalytical Empyrean X-ray diffractometer equipped with a 1.8 kW Cu K α ceramic X-ray tube, PIXcel3D 2x2 area detector and operating at 45 kV and 40 mA. The diffraction patterns were collected in air at room temperature using parallel-beam (PB) geometry and symmetric reflection mode. All XRD samples were prepared by drop casting a concentrated solution on a zero diffraction silicon wafer. The annealing was performed on drop-cast samples, heated on a hotplate in a glovebox. The X-ray diffraction spectra on the thin film for the solar cell were collected using a BRUKER D8 ADVANCE diffractometer with Bragg-Brentano geometry equipped with a Cu K α 1 (λ = 1.544060 Å) anode, at operating voltage of 40 kV and operating current of 40 mA. All diffraction patterns were collected at room temperature over an angular range (2θ) between 10° and 60°, step size 0.020° and acquisition time of 1 second. The sample was prepared by spin coating (1000 rpm, 60 s) with multiple step, as specified previously, on compact TiO₂/FTO).

J-V measurements setup. The current density-voltage (J-V) characteristics were measured with a computer-controlled Keithley 2400 source meter in air without any device encapsulation. The simulated Air Mass 1.5 Global (AM 1.5G) irradiance was provided with a class AAA Newport solar simulator. The light intensity was calibrated with a silicon reference cell with a spectral mismatch factor of 0.99. For the J-V measurement, the voltage step and delay time were 10 mV and 10 ms, respectively. The forward scan started from -0.5 V to 1.8 V, while reverse scan from 1.8 V to -0.5 V. The pre-condition for both scans was the same, that is, just with 5 s light exposure at 1.8 V. All devices were measured using a shadow mask of 0.0935 cm².

References

1. Boles, M. A., et al., The Surface Science of Nanocrystals. *Nat. Mater.* **2016**, *15*, 141-153.
2. Yang, J., et al., Designed Assembly and Integration of Colloidal Nanocrystals for Device Applications. *Adv. Mater.* **2016**, *28*, 1176-1207.
3. Kamat, P. V., Quantum Dot Solar Cells. Semiconductor Nanocrystals as Light Harvesters. *J. Phys. Chem. C* **2008**, *112*, 18737-18753.
4. Goodwin, E. D., et al., Effects of Post-Synthesis Processing on CdSe Nanocrystals and Their Solids: Correlation between Surface Chemistry and Optoelectronic Properties. *J. Phys. Chem. C* **2014**, *118*, 27097-27105.
5. Burda, C., et al., Chemistry and Properties of Nanocrystals of Different Shapes. *Chem. Rev.* **2005**, *105*, 1025-1102.
6. Donega, C. d. M., Synthesis and Properties of Colloidal Heteronanocrystals. *Chemical Society Reviews* **2011**, *40*, 1512-1546.
7. Peng, X., et al., Shape Control of CdSe Nanocrystals. *Nature* **2000**, *404*, 59-61.
8. Wang, R., et al., Colloidal Quantum Dot Ligand Engineering for High Performance Solar Cells. *Energy Environ. Sci.* **2016**, *9*, 1130-1143.
9. McDonald, S. A., et al., Solution-Processed Pbs Quantum Dot Infrared Photodetectors and Photovoltaics. *Nat. Mater.* **2005**, *4*, 138-142.
10. Li, G., et al., Efficient Light-Emitting Diodes Based on Nanocrystalline Perovskite in a Dielectric Polymer Matrix. *Nano Lett.* **2015**, *15*, 2640-2644.
11. Yoon, W., et al., Enhanced Open-Circuit Voltage of Pbs Nanocrystal Quantum Dot Solar Cells. *Sci. Rep.* **2013**, *3*, 2225.
12. Oh, S. J., et al., Engineering Charge Injection and Charge Transport for High Performance Pbse Nanocrystal Thin Film Devices and Circuits. *Nano Lett.* **2014**, *14*, 6210-6216.
13. Koleilat, G. I., et al., Efficient, Stable Infrared Photovoltaics Based on Solution-Cast Colloidal Quantum Dots. *ACS Nano* **2008**, *2*, 833-840.
14. Lan, X., et al., 10.6% Certified Colloidal Quantum Dot Solar Cells Via Solvent-Polarity-Engineered Halide Passivation. *Nano Lett.* **2016**, *16*, 4630-4634.
15. Zhang, H., et al., Solution-Processed, Ultrathin Solar Cells from CdCl₃-Capped Cdte Nanocrystals: The Multiple Roles of CdCl₃- Ligands. *J. Am. Chem. Soc.* **2016**, *138*, 7464-7467.
16. Saliba, M., et al., A Molecularly Engineered Hole-Transporting Material for Efficient Perovskite Solar Cells. *Nat. Energy* **2016**, *1*, 15017.
17. Saliba, M., et al., Cesium-Containing Triple Cation Perovskite Solar Cells: Improved Stability, Reproducibility and High Efficiency. *Energy Environ. Sci.* **2016**, *9*, 1989-1997.
18. Yang, W. S., et al., High-Performance Photovoltaic Perovskite Layers Fabricated through Intramolecular Exchange. *Science* **2015**, *348*, 1234-1237.
19. Cho, H., et al., Overcoming the Electroluminescence Efficiency Limitations of Perovskite Light-Emitting Diodes. *Science* **2015**, *350*, 1222-1225.
20. Ke, X., et al., Optical Band Gap Transition from Direct to Indirect Induced by Organic Content of CH₃NH₃PbI₃ Perovskite Films. *Appl. Phys. Lett.* **2015**, *107*, 091904.
21. Miyata, A., et al., Direct Measurement of the Exciton Binding Energy and Effective Masses for Charge Carriers in Organic-Inorganic Tri-Halide Perovskites. *Nat Phys* **2015**, *11*, 582-587.
22. Stranks, S. D., et al., Electron-Hole Diffusion Lengths Exceeding 1 Micrometer in an Organometal Trihalide Perovskite Absorber. *Science* **2013**, *342*, 341-344.
23. Giorgi, G., et al., Small Photocarrier Effective Masses Featuring Ambipolar Transport in Methylammonium Lead Iodide Perovskite: A Density Functional Analysis. *J. Phys. Chem. Lett.* **2013**, *4*, 4213-4216.
24. Koh, T. M., et al., Formamidinium-Containing Metal-Halide: An Alternative Material for near-Ir Absorption Perovskite Solar Cells. *J. Phys. Chem. C* **2014**, *118*, 16458-16462.
25. Zhang, W., et al., Enhanced Optoelectronic Quality of Perovskite Thin Films with Hypophosphorous Acid for Planar Heterojunction Solar Cells. *Nat. Commun.* **2015**, *6*, 10030.



26. He, H., et al., Exciton Localization in Solution-Processed Organolead Trihalide Perovskites. *Nat. Commun.* **2016**, *7*, 10896.
27. Nie, W., et al., High-Efficiency Solution-Processed Perovskite Solar Cells with Millimeter-Scale Grains. *Science* **2015**, *347*, 522-525.
28. Deschler, F., et al., High Photoluminescence Efficiency and Optically Pumped Lasing in Solution-Processed Mixed Halide Perovskite Semiconductors. *J. Phys. Chem. Lett.* **2014**, *5*, 1421-1426.
29. Schmidt, L. C., et al., Nontemplate Synthesis of $\text{CH}_3\text{NH}_3\text{PbBr}_3$ Perovskite Nanoparticles. *J. Am. Chem. Soc.* **2014**, *136*, 850-853.
30. Protesescu, L., et al., Nanocrystals of Cesium Lead Halide Perovskites (CsPbX_3 , X = Cl, Br, and I): Novel Optoelectronic Materials Showing Bright Emission with Wide Color Gamut. *Nano Lett.* **2015**, *15*, 3692-3696.
31. Tyagi, P., et al., Colloidal Organohalide Perovskite Nanoplatelets Exhibiting Quantum Confinement. *J. Phys. Chem. Lett.* **2015**, *6*, 1911-1916.
32. Sichert, J. A., et al., Quantum Size Effect in Organometal Halide Perovskite Nanoplatelets. *Nano Lett.* **2015**, *15*, 6521-6527.
33. Hu, F., et al., Superior Optical Properties of Perovskite Nanocrystals as Single Photon Emitters. *ACS Nano* **2015**, *9*, 12410-12416.
34. Bekenstein, Y., et al., Highly Luminescent Colloidal Nanoplates of Perovskite Cesium Lead Halide and Their Oriented Assemblies. *J. Am. Chem. Soc.* **2015**, *137*, 16008-16011.
35. Akkerman, Q. A., et al., Solution Synthesis Approach to Colloidal Cesium Lead Halide Perovskite Nanoplatelets with Monolayer-Level Thickness Control. *J. Am. Chem. Soc.* **2016**, *138*, 1010-1016.
36. Sun, S., et al., Ligand-Mediated Synthesis of Shape-Controlled Cesium Lead Halide Perovskite Nanocrystals Via Reprecipitation Process at Room Temperature. *ACS Nano* **2016**.
37. Bai, S., et al., Colloidal Metal Halide Perovskite Nanocrystals: Synthesis, Characterization, and Applications. *J. Mater. Chem. C* **2016**, *4*, 3898-3904.
38. De Roo, J., et al., Highly Dynamic Ligand Binding and Light Absorption Coefficient of Cesium Lead Bromide Perovskite Nanocrystals. *ACS Nano* **2016**, *10*, 2071-2081.
39. Swarnkar, A., et al., Quantum Dot-Induced Phase Stabilization of α - CsPbI_3 Perovskite for High-Efficiency Photovoltaics. *Science* **2016**, *354*, 92-95.
40. Stoumpos, C. C., et al., Crystal Growth of the Perovskite Semiconductor CsPbBr_3 : A New Material for High-Energy Radiation Detection. *Cryst. Growth Des.* **2013**, *13*, 2722-2727.
41. Sebastian, M., et al., Excitonic Emissions and above-Band-Gap Luminescence in the Single-Crystal Perovskite Semiconductors CsPbBr_3 and CsPbI_3 . *Phys. Rev. B* **2015**, *92*, 235210.
42. Akkerman, Q. A., et al., Tuning the Optical Properties of Cesium Lead Halide Perovskite Nanocrystals by Anion Exchange Reactions. *J. Am. Chem. Soc.* **2015**, *137*, 10276-10281.
43. Zorn, G., et al., Method for Determining the Elemental Composition and Distribution in Semiconductor Core-Shell Quantum Dots. *Analytical Chemistry* **2011**, *83*, 866-873.
44. Yakunin, S., et al., Low-Threshold Amplified Spontaneous Emission and Lasing from Colloidal Nanocrystals of Caesium Lead Halide Perovskites. *Nat. Commun.* **2015**, *6*, 8056.
45. Dou, L., et al., Atomically Thin Two-Dimensional Organic-Inorganic Hybrid Perovskites. *Science* **2015**, *349*, 1518-1521.
46. D'Innocenzo, V., et al., Tuning the Light Emission Properties by Band Gap Engineering in Hybrid Lead Halide Perovskite. *J. Am. Chem. Soc.* **2014**, *136*, 17730-17733.
47. Arora, N., et al., Photovoltaic and Amplified Spontaneous Emission Studies of High-Quality Formamidinium Lead Bromide Perovskite Films. *Adv. Funct. Mater.* **2016**, *26*, 2846-2854.
48. Yakunin, S., et al., Low-Threshold Amplified Spontaneous Emission and Lasing from Colloidal Nanocrystals of Caesium Lead Halide Perovskites. *Nat. Commun.* **2015**, *6*, 8056.
49. Xu, Y., et al., Two-Photon-Pumped Perovskite Semiconductor Nanocrystal Lasers. *J. Am. Chem. Soc.* **2016**, *138*, 3761-3768.

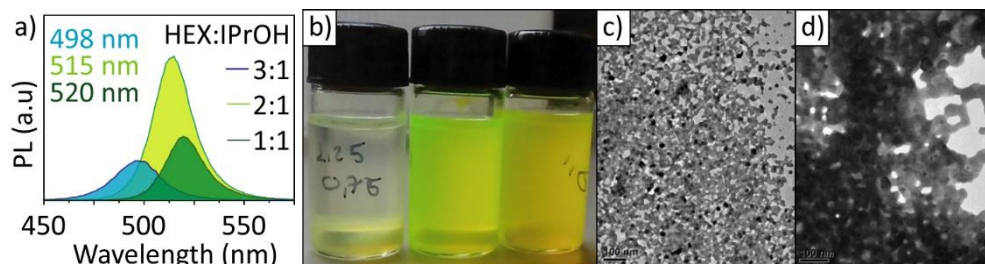
50. Vybornyi, O., et al., Polar-Solvent-Free Colloidal Synthesis of Highly Luminescent Alkylammonium Lead Halide Perovskite Nanocrystals. *Nanoscale* **2016**, *8*, 6278-6283.
51. Park, Y.-S., et al., Effect of Auger Recombination on Lasing in Heterostructured Quantum Dots with Engineered Core/Shell Interfaces. *Nano Lett.* **2015**, *15*, 7319-7328.
52. Gollner, C., et al., Random Lasing with Systematic Threshold Behavior in Films of CdSe/Cds Core/Thick-Shell Colloidal Quantum Dots. *ACS Nano* **2015**, *9*, 9792-9801.
53. Grim, J. Q., et al., Continuous-Wave Biexciton Lasing at Room Temperature Using Solution-Processed Quantum Wells. *Nat. Nano.* **2014**, *9*, 891-895.
54. Moreels, I., et al., Nearly Temperature-Independent Threshold for Amplified Spontaneous Emission in Colloidal CdSe/Cds Quantum Dot-in-Rods. *Adv. Mater.* **2012**, *24*, OP231-OP235.
55. Di Stasio, F., et al., Single-Mode Lasing from Colloidal Water-Soluble CdSe/Cds Quantum Dot-in-Rods. *Small* **2015**, *11*, 1328-1334.
56. Edri, E., et al., Chloride Inclusion and Hole Transport Material Doping to Improve Methyl Ammonium Lead Bromide Perovskite-Based High Open-Circuit Voltage Solar Cells. *J. Phys. Chem. Lett.* **2014**, *5*, 429-433.
57. Giesbrecht, N., et al., Synthesis of Perfectly Oriented and Micrometer-Sized Mapbbr3 Perovskite Crystals for Thin-Film Photovoltaic Applications. *ACS Energy Lett.* **2016**, *1*, 150-154.
58. Arora, N., et al., High Open-Circuit Voltage: Fabrication of Formamidinium Lead Bromide Perovskite Solar Cells Using Fluorene-Dithiophene Derivatives as Hole-Transporting Materials. *ACS Energy Lett.* **2016**, *1*, 107-112.
59. Kulbak, M., et al., Cesium Enhances Long-Term Stability of Lead Bromide Perovskite-Based Solar Cells. *J. Phys. Chem. Lett.* **2016**, *7*, 167-172.
60. Sutton, R. J., et al., Bandgap-Tunable Cesium Lead Halide Perovskites with High Thermal Stability for Efficient Solar Cells. *Adv. Energy Mater.* **2016**, *6*, 1502458-n/a.
61. Gao, P., et al., Organohalide Lead Perovskites for Photovoltaic Applications. *Energy Environ. Sci.* **2014**, *7*, 2448-2463.
62. Shockley, W.; Queisser, H. J., Detailed Balance Limit of Efficiency of P-N Junction Solar Cells. *J. Appl. Phys.* **1961**, *32*, 510-519.
63. Kulbak, M., et al., How Important Is the Organic Part of Lead Halide Perovskite Photovoltaic Cells? Efficient CsPbBr₃ Cells. *J. Phys. Chem. Lett.* **2015**, *6*, 2452-2456.
64. Ryu, S., et al., Voltage Output of Efficient Perovskite Solar Cells with High Open-Circuit Voltage and Fill Factor. *Energy Environ. Sci.* **2014**, *7*, 2614-2618.
65. Lignos, I., et al., Exploration of near-Infrared-Emissive Colloidal Multinary Lead Halide Perovskite Nanocrystals Using an Automated Microfluidic Platform. *ACS Nano* **2018**, *12*, 5504-5517.
66. Protesescu, L., et al., Dismantling the “Red Wall” of Colloidal Perovskites: Highly Luminescent Formamidinium and Formamidinium-Cesium Lead Iodide Nanocrystals. *ACS Nano* **2017**, *11*, 3119-3134.
67. Ball, J. M., et al., Low-Temperature Processed Meso-Superstructured to Thin-Film Perovskite Solar Cells. *Energy Environ. Sci.* **2013**, *6*, 1739-1743.
68. Helander, M. G., et al., Pitfalls in Measuring Work Function Using Photoelectron Spectroscopy. *Appl. Surf. Sci.* **2010**, *256*, 2602-2605.
69. Calloni, A., et al., Stability of Organic Cations in Solution-Processed CH₃NH₃PbI₃ Perovskites: Formation of Modified Surface Layers. *J. Phys. Chem. C* **2015**, *119*, 21329-21335.
70. Schulz, P., et al., Interface Energetics in Organo-Metal Halide Perovskite-Based Photovoltaic Cells. *Energy Environ. Sci.* **2014**, *7*, 1377-1381.
71. de Mello, J. C., et al., An Improved Experimental Determination of External Photoluminescence Quantum Efficiency. *Adv. Mater.* **1997**, *9*, 230-232.

Appendix table 11.1. Performances of the NCs-based perovskite solar cells, depending on the number of the deposited layers. Scan direction “Reverse” means open circuit voltage to short circuit; “Forward” means from short circuit to open circuit voltage. 10ms delay between two polarization steps.

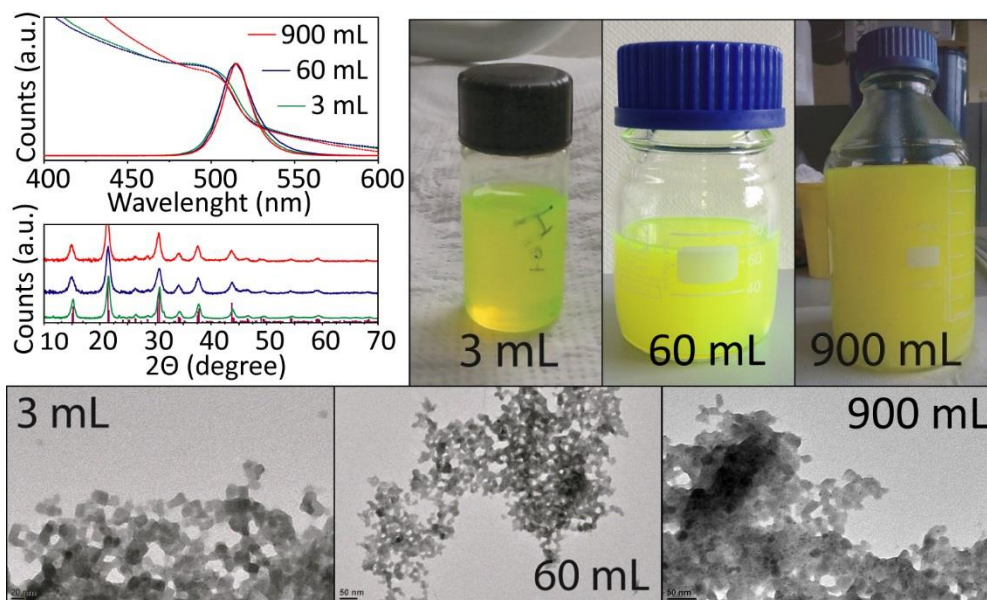
N° Deposition cycles	Scan direction	J_{sc} (mA cm ⁻²)	V_{oc} (V)	FF	PCE (%)
1	Reverse	1.385	0.845	0.575	0.67
1	Forward	1.296	0.843	0.504	0.55
2	Reverse	1.836	0.942	0.650	1.12
2	Forward	1.740	0.921	0.598	0.96
3	Reverse	3.182	1.151	0.627	2.30
3	Forward	2.779	1.064	0.506	1.50
6	Reverse	3.964	1.209	0.521	2.50
6	Forward	3.419	1.126	0.457	1.76
7	Reverse	4.090	1.405	0.638	3.67
7	Forward	3.469	1.315	0.488	2.22
8	Reverse	4.367	1.403	0.639	3.91
8	Forward	3.700	1.302	0.491	2.37
9	Reverse	5.653	1.536	0.624	5.42
9	Forward	4.766	1.306	0.381	2.37
10	Reverse	5.369	1.448	0.565	4.39
10	Forward	4.464	1.268	0.367	2.08
12	Reverse	5.512	1.505	0.628	5.20
12	Forward	4.373	1.287	0.375	2.11
14	Reverse	5.289	1.455	0.614	4.73
14	Forward	4.171	1.228	0.386	1.97

Appendix table 11.2. Figures of merit relative to the J-V characteristics reported in

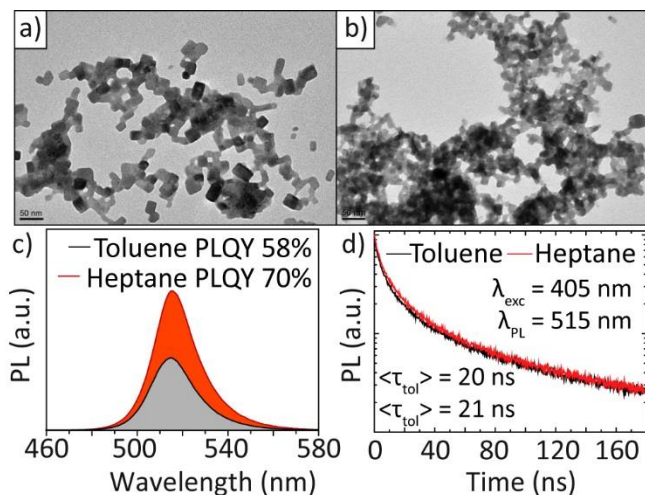
Meas. delay (ms)	Scan direction	J_{sc} (mA cm ⁻²)	V_{oc} (V)	FF	PCE (%)
10	Reverse	3.526	1.293	0.670	3.05
10	Forward	2.904	1.237	0.483	1.77
6000	Reverse	4.045	1.185	0.639	3.07
6000	Forward	4.021	1.207	0.631	3.06



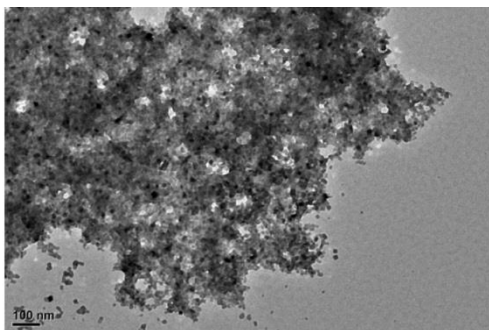
Appendix 11.1: CsPbBr₃ NCs synthesized at different HEX:IPrOH ratios. (a) Effect HEX:IPrOH ratios on PL of NCs. (b) photos of NCs synthesized with HEX:IPrOH ratios. TEM images of (c) smaller and (d) larger NC domains, compared to the standard synthesis.



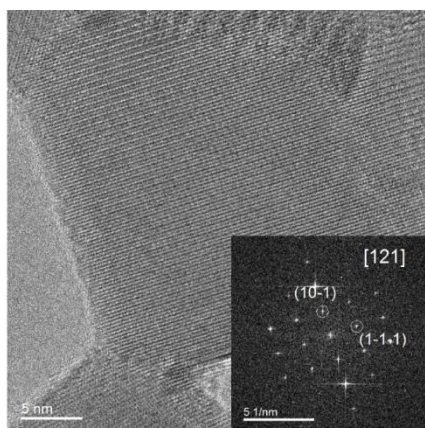
Appendix 11.2. Overview of properties of NCs prepared by milligram-scale (3 mL and 60 mL) and gram-scale syntheses (900 mL).



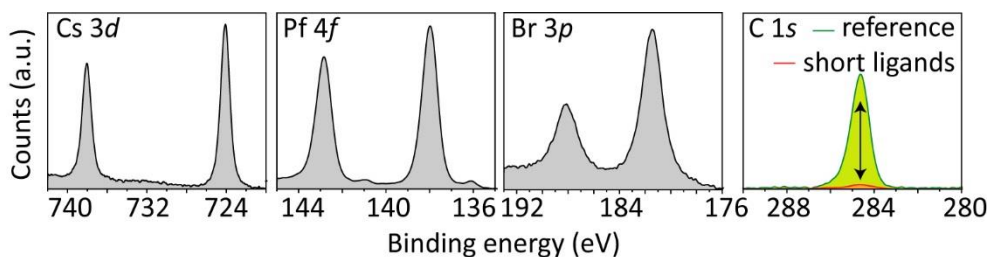
Appendix 11.3. CsPbBr₃ NC inks obtained using heptane. TEM image (a and b) of CsPbBr₃ NCs synthesized using heptane as non-polar solvent. (c) Steady-state PL spectra of two different NCs batches synthesized using either toluene (black solid line) or heptane (red solid line) as solvent. (d) time-resolved PL measured at the PL peak ($\lambda=515 \text{ nm}$) for the two NCs batches.



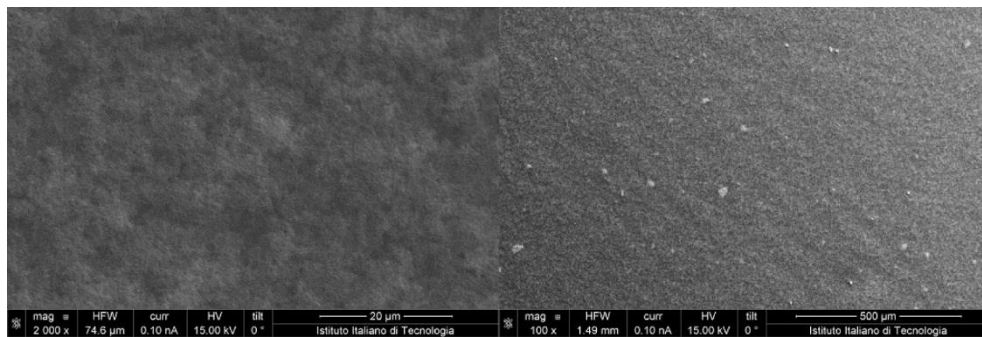
Appendix 11.4. TEM image of NCs as obtained from the synthesis, before washing.



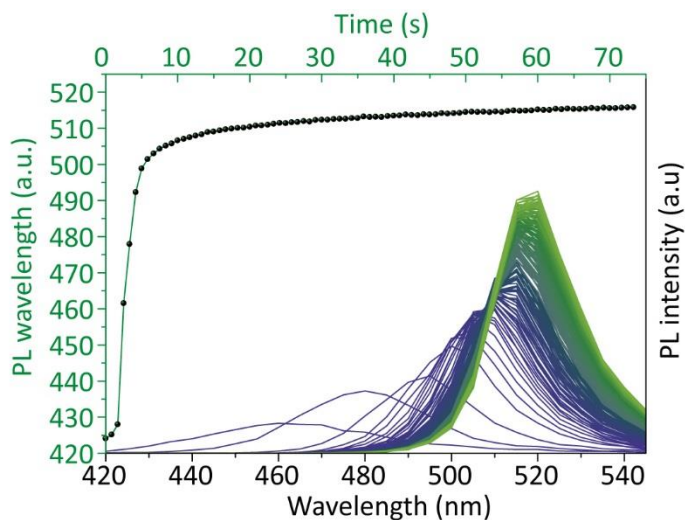
Appendix 11.5. HRTEM image of CsPbBr₃ NCs.



Appendix 11.6. Selected regions of XPS spectra, from which a Cs:Pb:Br ratio of 0.90:1.00:3.00 was extracted. The last panel compares the carbon signal from a reference sample of 8.5 nm CsPbBr₃ cubes prepared with the traditional synthesis procedure of Protesescu *et al.*¹ (green) and from a sample of NCs inks prepared with our approach (red). The sample prepared with our approach contained 25 times less carbon than the “traditional” sample.

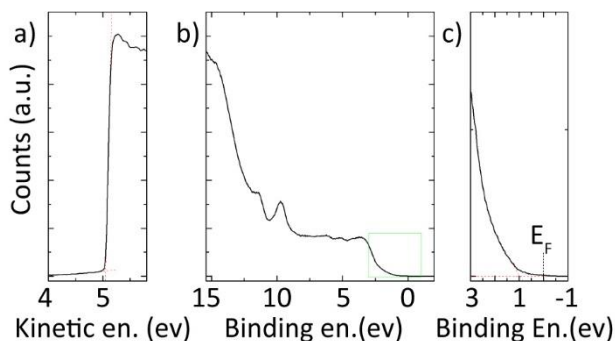


Appendix 11.7. SEM images (at two different magnifications) of a uniform film prepared by spin-coating the NC ink.

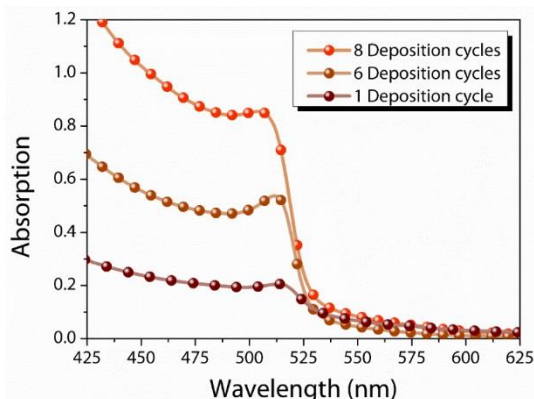


Appendix 11.8. PL spectra measurements of the synthesis recorded over 75 seconds, with an interval of 0.8 second from each spectrum to the next. The growth essentially stopped after the first 10-20 seconds.

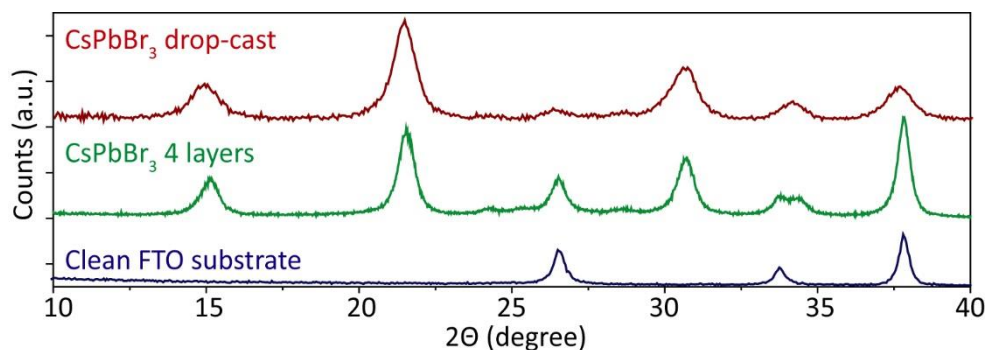




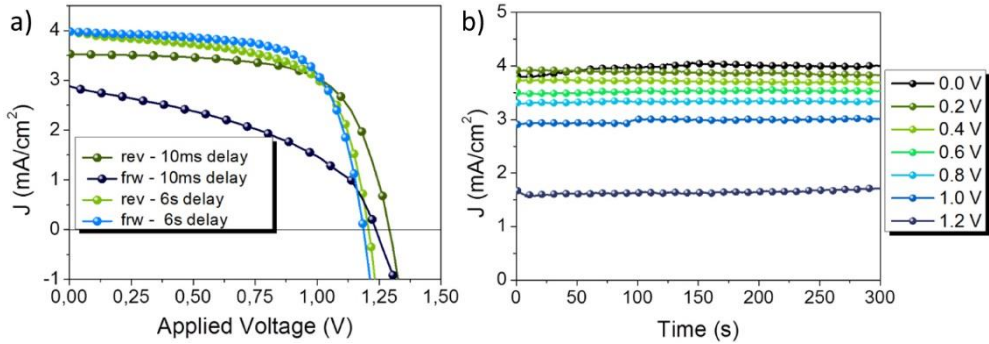
Appendix 11.9: Representative UPS spectrum of CsPbBr₃ NC inks spin-cast on a silicon wafer. (a) Intensity of secondary electron emission upon He I excitation, as a function of the kinetic energy of the photoelectrons. The photoemission onset is directly correlated with the work function (WF) of the material. For the CsPbBr₃ NC inks, WF = (5.05 ± 0.05) eV were calculated. **(b)** UPS valence band. The region close to the Fermi level (E_F) (marked with the green box) is magnified in panel **(c)**, showing the position of the valence band maximum (VBM) at (1 ± 0.1) eV below E_F . The position of VBM with respect to the vacuum level is therefore (-6.05 ± 0.12) eV.



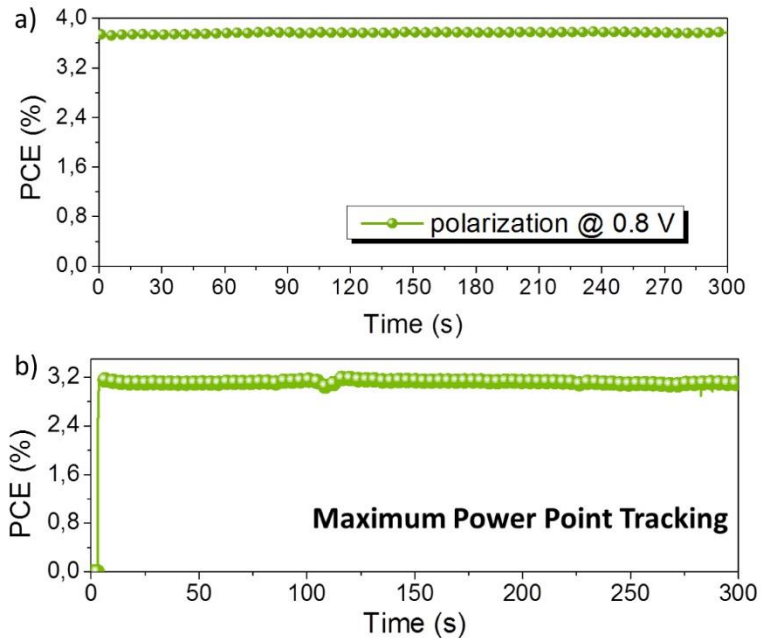
Appendix 11.10: Absorption spectra of CsPbBr₃ sequential deposition cycles (8, 6 and 1) on compact TiO₂/FTO.



Appendix 11.11: XRD spectra of 4 NC ink deposition cycles (green) compared to a drop cast film of CsPbBr₃ (red), deposited on compact TiO₂/FTO. As a reference, a clean FTO substrate spectrum (blue) is shown.

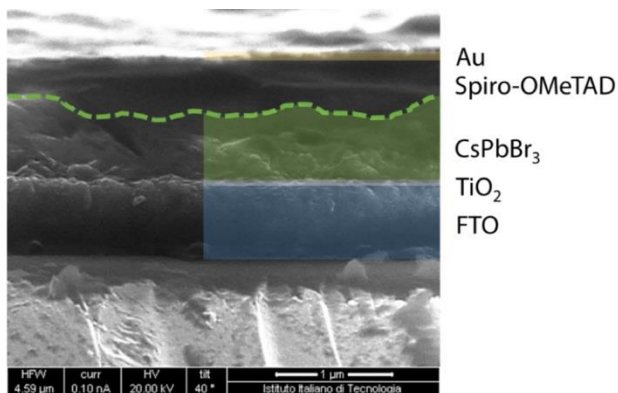


Appendix 11.12: Example of Current Density-voltage characteristics for a photovoltaic devices FTO/c-TiO₂/CsPbBr₃/spiro-MeOTAD/Au under AM 1.5G white light illumination with an intensity of approximately 100 mW/cm². (a) The perovskite thin films correspond to deposition cycles. (OD 0.6). Upon about 1s illumination the device is electrically stable. (b) Transient photo-current density upon different polarizations.

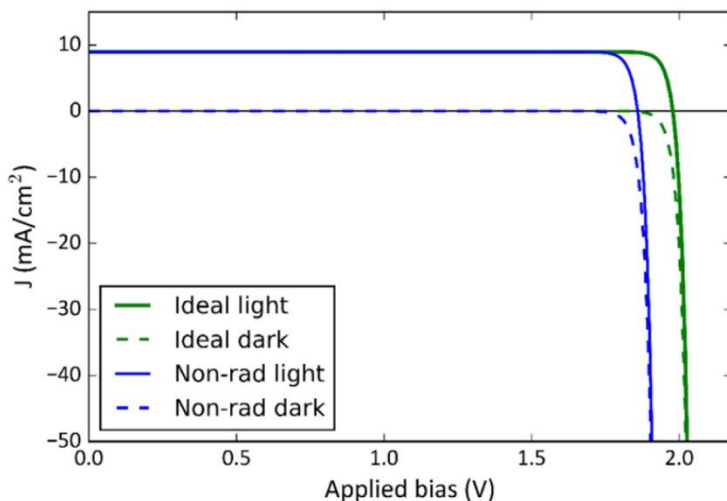


Appendix 11.13: Additional data from CsPbBr₃ NC solar cell. (a) Stabilized PCE at 0.8V polarization. (b) PCE at maximum power point measured through Maximum power point tracking method.

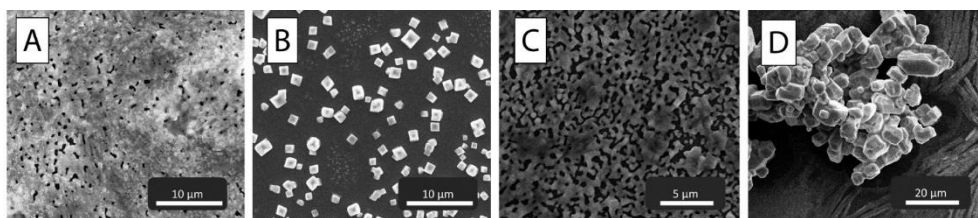




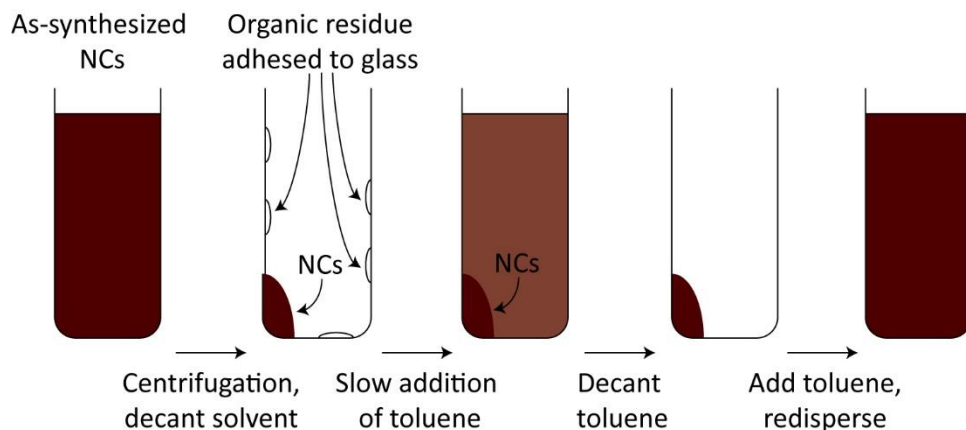
Appendix 11.14. Cross-section scanning electron microscopy image of a solar cell prepared with 8 spin-coating deposition cycles of CsPbBr₃.



Appendix 11.15. Calculated Current-Voltage characteristics of ideal CsPbBr₃ solar cell (in green) and considering non radiative recombination in the semiconductor (in blue).



Appendix 11.16. SEM images of CsPbBr₃ thin films fabricated with a range of state-of-the-art processing protocols. (a) One step deposition with a DMF-based solvent annealing step (adapted from Rebecca J. Sutton et al.)²; (b) one step deposition with low temperature annealing (Rachel E. Beal et al.)³; (c) one step deposition (adapted from Rebecca J. Sutton et al.)²; (d) hot casting technique (adapted from Wanyi Nie et al.)⁴.

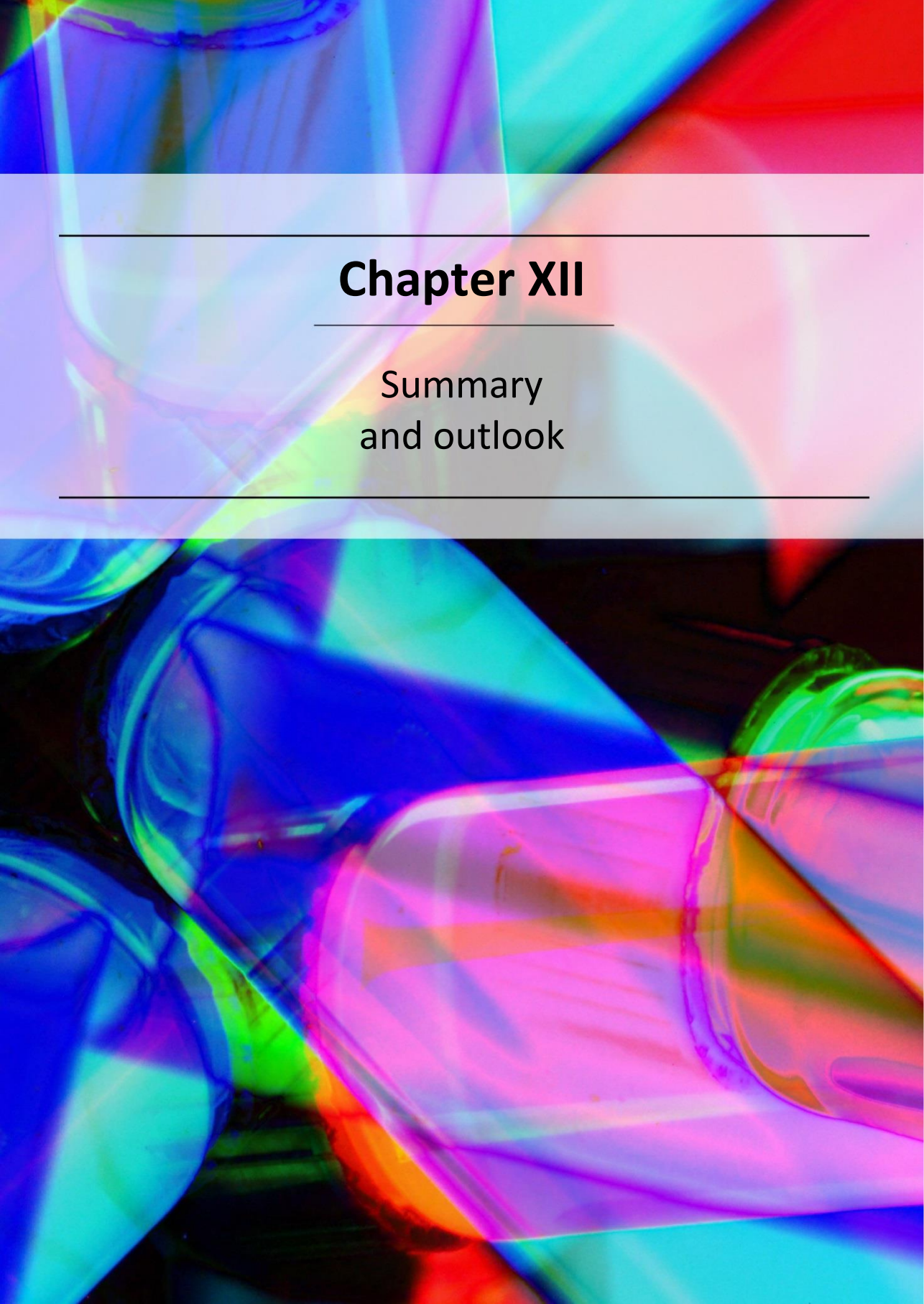


Appendix 11.17. Schematic representation of the 'rinsing' procedure of the NCs

1. Protesescu, L., et al., Nanocrystals of Cesium Lead Halide Perovskites (CsPbX_3 , X = Cl, Br, and I): Novel Optoelectronic Materials Showing Bright Emission with Wide Color Gamut. *Nano Lett.* **2015**, *15*, 3692-3696.
2. Sutton, R. J., et al., Bandgap-Tunable Cesium Lead Halide Perovskites with High Thermal Stability for Efficient Solar Cells. *Adv. Energy Mater.* **2016**, *6*, 1502458-n/a.
3. Beal, R. E., et al., Cesium Lead Halide Perovskites with Improved Stability for Tandem Solar Cells. *J. Phys. Chem. Lett.* **2016**, *7*, 746-751.
4. Nie, W., et al., High-Efficiency Solution-Processed Perovskite Solar Cells with Millimeter-Scale Grains. *Science* **2015**, *347*, 522-525.







Chapter XII

Summary
and outlook

Chapter XII: Summary and outlook

Abstract: *In this thesis, several aspects of lead halide perovskite nanocrystals have been discussed. It has been shown that that changing the size, shape and composition of lead halide perovskite nanocrystals not only strongly influences the optical properties, but can also increase the stability (chapters 5 and 6). In chapters 7-9, it was demonstrated that several other lead halide phases, like OD Cs_4PbX_6 and the Ruddlesden Popper phase $Cs_2PbI_2Cl_2$ nanocrystals, can also be synthesized on the nano-scale, but they exhibit very different optical properties from their lead halide perovskite nanocrystal counterparts. This thesis has also presented a novel synthesis method for other iodide based nanocrystals (as opposed to lead halide perovskite nanocrystals), which should create opportunities for a general exploration of halide based nanocrystals. Finally, it was shown that the synthesis of $CsPbBr_3$ nanocrystals can be tuned for their use in applications, by directly removing bulky long ligands and replacing them with shorter ones, allowing for them to be used in solar cells that operate at a high voltage.*

12.1 Lead halide perovskite nanocrystals

One of the newest entries to the semiconductor NC family is the lead halide perovskite NC. This type of NC quickly gained interest in the scientific community owing to its ease of synthesis and optical tunability as well as its very high optical properties. Despite the fact that these NCs have been intensively studied and that they are now among the most investigated semiconducting NCs, several physical and optical features have yet to be discovered. Although the work presented in this thesis provides information on some of the properties of this material, there is still much to be gained from continuing work in this field.

12.2 Size, shape and compositional control

In the first part of this thesis (*Chapters 5 and 6*), the size, shape and compositional tuning of LHP NCs was discussed. It was shown that $CsPbBr_3$ NCs could be synthesized as ultrathin nanoplatelets by altering the acidity of the reaction. These NPLs showed a strongly blue shifted PL compared to cubically shaped $CsPbBr_3$ NCs, and they also exhibited a strong excitonic absorption, both of which indicate that a strong quantum confinement is forced upon the NPLs. Furthermore, it was shown that the shape tunability was a result of the increased acidity, consequently leading to an increase in the concentration of oleylammonium, which partially promotes the anisotropic growth of $CsPbBr_3$. Furthermore, it has been demonstrated that the composition of $CsPbCl_3$ and $CsPbI_3$ can be easily tuned by alloying them with Mn^{2+} . When $CsPbCl_3$ was alloyed with Mn^{2+} , the PL strongly downshifted, originating from the ${}^4T_1 \rightarrow {}^6A_1$ optical transition of the Mn^{2+} . When $CsPbI_3$ NCs were alloyed with Mn^{2+} , there was no evidence of any alterations of the optical properties, as the Mn^{2+} levels fall within the conduction band. However, alloying $CsPbI_3$ with Mn^{2+} allows for a small decrease in the lattice parameters, which slightly increases the Goldsmith tolerance factor, thus preventing the $CsPbI_3$ NCs from degrading into the δ - $CsPbI_3$ phase. These alloyed NC films and NCs in solution are stable for over a month, therefore they are much more stable than their parent $CsPbI_3$, which is only stable for a few days.

12.3 The different phases of cesium lead halides nanocrystals

As was discussed in *chapters 7 to 9*, cesium lead halides can crystalize in several phases other than in the CsPbX_3 phase. One of these phases, the Cs_4PbX_6 phase, consists of disconnected, single PbX_6^{4-} octahedra surrounded by Cs^+ atoms. The decoupling of the lead halide octahedra leads to very large bandgaps, similar to those of free PbX_6^{4-} either in solution or doped in large bandgap matrices. In this thesis, the synthesis of nearly monodisperse Cs_4PbX_6 NCs was presented, and their optical properties were compared to those of LHP NCs. One of the most interesting features of Cs_4PbX_6 NCs is that they are easy to transform into CsPbBr_3 NCs. These transformations preserve the size of the starting Cs_4PbX_6 NCs, and results in luminescent, monodisperse CsPbBr_3 NCs. This thesis also discusses the debate on where the green luminescence in several reported Cs_4PbX_6 bulk powders and single crystals originates from. Due to the observed properties of this green luminescence, such as its narrow PL, small stokes shift, and high PLQY, it is likely that the green PL originate from small CsPbBr_3 NC-like impurities.

The second type of non-perovskite cesium lead halide NCs discussed in this thesis is fully inorganic Ruddlesden Popper phase NCs. These NCs, in the form of $\text{Cs}_2\text{PbI}_2\text{Cl}_2$, form NPLs, and they consist of a single layer of corner sharing Pb-Cl octahedra, which are terminated with iodide ions at the axial positions. These NCs exhibit a highly excitonic absorption spectrum due the strong quantum confinement within the single Pb-Cl layers. Finally, $\text{CsPb}(\text{Cl}:\text{Br}:\text{I})_3$ NCs containing all three halides were synthesized. Although these NCs crystalized in the cubic perovskite structure, they exhibit several RPP planes per NC, and this is similar to $\text{Cs}_2\text{PbI}_2\text{Cl}_2$. The formation of these RPP planes is driven by the segregation of the larger iodide halides. This iodide segregation does not only lead to the formation of RPP planes, but it also leads to the generation of charge traps in the electronic structure of the NC, consequently quenching the PL.

12.4 Towards novel synthesis approaches and high quality lead halide perovskite nanocrystal devices

The last two experimental chapters of this thesis described two new synthesis methods for metal iodide NCs and CsPbBr_3 NC inks. The metal iodide NCs were synthesized by injecting a solution of oleylammonium iodide, which had been formed *in situ*, into a mixture of different metal (and inorganic) oleates. This led to the formation of a wide range of iodide NCs, including KI, RbI, CsI, AgI, CsPbI_3 , FAPbI_3 , Cs_4PbI_6 , Cs_3BiI_9 , FA_3BiI_9 and RbAg_4I_5 NCs. In the case of the CsPbI_3 and FAPbI_3 NCs, their high PLQYs were utilized for the fabrication of red and NIR emitting LEDs, which exhibited performances that are similar to the current record for NC LEDs. The second new synthesis method utilizes the use of short ligands and solvents with low boiling points, allowing for the synthesis of CsPbBr_3 NC inks which can directly be used for high quality, device ready, NC films. These NC inks were used for the fabrication of CsPbBr_3 NC-based solar cells, which had efficiencies above 5% and open-circuit voltages as high as 1.5 V, which is currently among the highest for LHP solar cells.

12.5 Outlook

This thesis provides new insight into the synthesis, optical properties and potential applications of LHP and other metal halide based NCs. However, there are still many challenges to overcome before LHP NCs can be used in consumer devices.

One of the main problems with LHP NCs is that they contain lead, which is an extremely toxic metal. Due to the highly polar nature of LHPs, they can be easily dissolved in polar solvents (like water), leading to serious health and safety issues. So far, no feasible alternatives have been found for replacing lead in these NCs, as most replacements lead to stability issues, decreases in the PLQY, large Stokes shifts, and a significant broadening of the PL. Thus, future work on LHPs will mainly focus on finding sufficient replacements for lead.

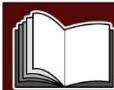
Again, due to the highly polar nature of the LHP NCs, it is extremely difficult to epitaxially grow other materials on top of LHP NCs. One interesting development would be to find the right reaction conditions for the synthesis of core-shell LHP NCs, either by using LHPs as a shell for NCs with a narrow bandgap, like PbSe, for highly emissive IR NCs, or by using LHPs as a core with a chemically robust shell, like ZnS or silica.

List of abbreviations

0/1/2/3D	0/1/2/3 Dimensional	LSPR	Localized Surface Plasmon Resonance
Abs	Absorption	LUMO	Lowest Unoccupied Molecular Orbital
AM1.5	1.5 Times Air Mass	MA	Methylammonium
AO	Atomic Orbital	ML	Mono Layer
ASE	Amplified Spontaneous Emission	MO	Molecular Orbital
BBI	Broad Band Inverse Probe	NCs	Nanocrystal
BE	Band Edge	NIR	Near Infra-Red
BuAm	Butylamine	NMR	Nuclear Magnetic Resonance
CB	Conduction Band	NPLs	Nanoplatelets
CIE	Color Rendering Index	NSs	Nanosheets
CNT	Classic Nucleation Theory	OA	Oleic Acid
DDDA	Didodecylamine	ODE	1-Octadecene
DFT	Density Functional Theory	OLAM	Oleylamine
DMF	Dimethyl Formamide	PB	Parallel Beam
DOS	Density of States	PBE	Perdew-Burke-Ernzerhof
DPE	Diphenyl Ether	PCE	Power Conversion Efficiency
EDBE	2,2'-(Ethylenedioxy)Bis(Ethylammonium)	PDOS	Projected Density Of States
EDS	Energy-Dispersive X-Ray Spectroscopy	PEDOT:PSS	Poly(3,4-Ethylenedioxythiophene)-Poly(Styrenesulfonate)
EDX	Energy-Dispersive X-Ray Spectroscopy	PL	Photoluminescence
EQE	External Quantum Efficiency	PLE	Photoluminescence Excitation
FA	Formamidinium	PLQY	Photoluminescence Quantum Yield
FF	Fill Factor	PO-T2T	2,4,6-Tris[3-(Diphenylphosphinyl)Phenyl]-1,3,5-Triazine
FIDs	Free Induction Decays	PrAc	Propionic Acid
FWHM	Full Width at Half Maximum	PV	Photovoltaics
HAADF	High-Angle Annular Dark-Field	QD	Quantum Dot
HEX	Hexane	RoHS	Restriction of Hazardous Substances
HOMO	Highest Occupied Molecular Orbital	RT	Room Temperature
HRTEM	High Resolution transmission electron microscopy	SEM	Scanning Electron Microscope
HSE	Heyd-Scuseria-Ernzerhof	Ss	Stokes Shift
ICP	Inductively Coupled Plasma Optical Emission Spectroscopy	SOC	Spin-Orbit Coupling
IPrOH	Isopropanol	Spiro-MeOTAD	2,2',7,7'-Tetrakis-(N,N-P Dimethoxyphenylamino)-9,9'-Spirobifluorene
IR	Infra-red	SR	Scalar Relativistic
ITO	Indium Tin Oxide	STEM	Scanning Transmission Electron Micrograph
J_{sc}	Circuit Values	STEM	Scanning Transmission Electron Microscope
LCAO	Linear Combination of Atomic Orbitals	SUHD	Samsung Ultra High Definition
LCD	Liquid-Crystal Displays	TA	Transient Absorption
LCD	Liquid-Crystal Displays		
LED	Light Emitting Diode		
LHP	Lead Halide Perovskite		

TCSPC Time-Correlated Single Photon
Counting
TDDFT Time-Dependent Density
Functional theory
TEM Transmission Electron Microscopy
TOL Toluene
TOP Trioctylphosphine
UPS Ultraviolet Photoelectron
Spectroscopy

UV Ultra Violet
VB Valence Band
VBM Valence Band Maximum
Vis Visible
V_{oc} Open Circuit Voltage
V_x X Vacancy
WF Work Function
XRD X-Ray Diffraction



Acknowledgments

More than 70000 words, and over a 100 figures later, my thesis, and therefore my PHD, is drawing to an end. While I am writing these final words, I find myself thinking back on the four incredible years I've had here at IIT, as well as in Genova. I would not have had such a positive experience here if it had not have been for the many people I have met along the road. Therefore, I would like to thank the following people; thank you to everyone mentioned below for shaping the past four years into a truly incredible experience.

I would like to start by thanking **Liberato Manna** (the supreme leader), my main supervisor and the head of the Nanochemistry department at IIT. Without him, I never would have started my PhD at IIT (through UniGe), therefore I would not have achieved all that I have managed to today. The first time I met "Liberato" was more than a year before I actually started my PhD, when I conducted an internship in his group as part of my master degree. Now, more than four and a half years later, it is time to say goodbye and move on. I would like to thank him for giving me the chance to work in your group and for all your help, supervision and support throughout these years. A special thanks also to **Mirko Prato** who, as my co-supervisor at IIT, helped me a lot at the beginning of my PhD.

Throughout the years here at IIT, many of my colleagues across various departments have become close friends. I thank **Ahmed L Abdelhady, Guilherme Almeida, Sedat Dogan, Umair Gulzar, Arjen Boender, Muhammad Imran, Francisco Palazon, Sungwook Park, Taimoor Masood, Amira El Merhie** and **Dmitry Baranov** not only for making IIT such an enjoyable place to work but also for making my stay in Genova so much more fun! I would like to also thank my friends from outside of IIT. From back home, in The Netherlands, **Joris Scheers, Justin Mieras, Teun Steur** and **Paul van Riet**, who came to visit me in Genova several times as well as **Tim Hamelink**. There are also several friends to thank who I met outside IIT (**Mohsen Shiee** and **Masha Dvoriashyna**), whose company during my free time was a lot of fun.

My work at IIT would not have been possible without the help of the many important staff members. I give a big thanks to **Iulia Manolache Orlatan**, as well as **Joke Huyghebaert** and **Edith Torres**, who dealt with all the administration work, making my stay at IIT, as well as my travel plans with regard to conferences all around the world, so much easier. The work in the lab, of course, would not have been possible without the help of all the excellent technicians, including **Simone Nitti, Gabriele La Rosa, Giammarino Pugliese, Filippo Drago** and **Francesco De Donato**, who always helped me out with all chemicals and glassware I needed, as well as with shipping samples and performing measurements. A big thanks to all other staff members and researchers at IIT who helped me to run measurements and who trained me on how to properly use the equipment at IIT, including **Sergio Marras, Luca Goldoni, Zhiya Dang, Giovanni Bertoni, Alice Scarpellini** and **Rosaria**.

There are also a lot of internal and external collaborators I have had the joy and honor to work with over the few past years: **Abhinav Anand, Ajay Ram Srimath Kandada, Ali Hossain Khan, Annamaria Petrozza, Carmine Urso, Clemens Burda, Daniele Meggiolaro, Davide Sciacca, Edoardo Mosconi, Emory Chan, Eros Radicchi, Eva Bladt, Fang Chen, Federico Locardi, Filippo De Angelis, Francesca Nunzi, Francesco Di Stasio Francesco**

Meinardi, Francesco Tassone, Gabriele Rainò, Henk J Bolink, Ilaria Nelli, Ivan Infante, Iwan Moreels, Jacopo Pedrini, James M Ball, Javad Shamsi, Laura Martínez-Sarti, Luca De Trizio, Luca Sortino, Maksym Kovalenko, Marco Fanciulli, Marina Gandini, Maurizio Ferretti, Monica Lorenzon, Prachi Rastogi, Roman Krahne, Sara Accornero, Sara Bals, Sergio Brovelli, Silvia Genaro Motti, Stefanie Neutzner, Urko Petralanda, Valerio D’Innocenzo, and Valerio Pinchetti. Thank you for all the amazing scientific work you involved me in!

Throughout my PhD, I had the pleasure of supervising two very smart and friendly students, **Emanuela Sartori** and **Rian Ligthart**. Not only did you help me to improve my supervisory skills, but you also helped me a lot with my research and I am looking forward to meeting you again sometime in the future when our paths cross again.

Without a doubt, I would also like to say thanks to my my parents **Jaap Akkerman** and **Jen Haase** as well as my sister **Olly Akkerman**, all of whom came to visit me many times here. Having your support after leaving home to live abroad means the world to me.

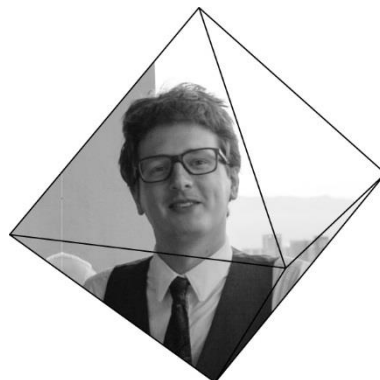
Finally, I want to thank my fiancée (aka *future wife*) **Emma De Cecco**. Not only did she actually contribute to this thesis by reading through hundreds of pages and correcting the English on pretty much every single one, but you also stuck around and were supportive throughout the most stressful parts of my PhD. You were always there for me, even when I was working late nights, responding to midnight emails or skype calls, traveling around the world for conferences and collaborations, or spending weekends in the lab. I would like to thank you for this, and I’m looking forward to wherever our next adventure brings us. I love you.

So here it is, the end of my thesis. Another, final thanks to all the above mentioned people, and I will always look fondly back on my time here in Genova!



About the author

Quinten Adriaan Akkerman was born on the 7th of November in Haarlem, The Netherlands. He obtained his pre-university degree at the Goese Lyceum in Goes, before moving to Utrecht in 2008 to study Chemistry at the University of Utrecht. In 2012, he obtained his Bachelor's degree after finishing his research project under the supervision of Wiel Evers, in Daniel Vanmaekelberg's group. Here, he conducted research on colloidal semiconductor NCs for the first time, with the aim of self-assembling CdSe and CdS NCs into binary self-assemblies. In 2012, he started his Master's degree in Chemistry and Physics, also at the University of Utrecht, and he carried out his Master's project as a member of Celso de Mello Donegá's group. During this project, Quinten worked on the size, shape and compositional control of copper chalcogenide nanocrystals under the supervision of Ward van der Stam. His research here contributed to three publications. During this Master's program, Quinten participated in a 5 month internship at the Istituto Italiano di Tecnologia (IIT) Genova, Italy, in Liberato Manna's group. Here, he worked on cation exchange reactions on Copper sulfide NCs, mainly with the aim of synthesizing luminescent CuInS₂ nanocrystals. The research he conducted during this placement resulted in a fourth publication, this time as the first author, in ACS Nano. After finishing his Internship, he graduated Cum Laude and with honors in 2014.



After his successful internship, Quinten rejoined Liberato Manna's group again in 2015, this time as a PhD student. At the start of his PhD, he began to work on lead halide perovskite nanocrystals, focusing on different synthetic aspects like composition and shape control, and the results of this research are described in this thesis. During his PhD, he published seven papers as the first author, and contributed to 16 more papers. He has also supervised two students. He has been awarded the *Excellent Shotgun Presentation Award*, the *Nature Nanotechnology best student poster in nanotechnology award* and the *RSC Journal of Materials Chemistry A poster prize award* at the ISN2A 2016, PSCO 2016, and AP-HOPV17 conferences respectively. Finally, he has been an invited speaker at two international conferences (Colloidal Semiconductor Nanocrystals (GRS), and E-MRS Fall Meeting).

Publications

As first author:

Akkerman, Q. A.; Motti, S. G.; Srimath Kandada, A. R.; Mosconi, E.; D’Innocenzo, V.; Bertoni, G.; Marras, S.; Kamino, B. A.; Miranda, L.; De Angelis, F.; Petrozza, A.; Prato, M.; Manna, L., **Solution Synthesis Approach to Colloidal Cesium Lead Halide Perovskite Nanoplatelets with Monolayer-Level Thickness Control.** *J. Am. Chem. Soc.* **2016**, *138*, 1010-1016.

Akkerman, Q. A.; Gandini, M.; Di Stasio, F.; Rastogi, P.; Palazon, F.; Bertoni, G.; Ball, J. M.; Prato, M.; Petrozza, A.; Manna, L., **Strongly Emissive Perovskite Nanocrystal Inks for High-Voltage Solar Cells.** *Nat. Energy* **2016**, *2*, 16194.

Akkerman, Q. A.; Park, S.; Radicchi, E.; Nunzi, F.; Mosconi, E.; De Angelis, F.; Brescia, R.; Rastogi, P.; Prato, M.; Manna, L., **Nearly Monodisperse Insulator Cs₄PbX₆ (X = Cl, Br, I) Nanocrystals, Their Mixed Halide Compositions, and Their Transformation into CsPbX₃ Nanocrystals.** *Nano Lett.* **2017**, *17*, 1924-1930.

Akkerman, Q. A.; Meggiolaro, D.; Dang, Z.; De Angelis, F.; Manna, L., **Fluorescent Alloy CsPb_xMn_{1-x}I₃ Perovskite Nanocrystals with High Structural and Optical Stability.** *ACS Energy Lett.* **2017**, *2*, 2183-2186.

Akkerman, Q. A.; Abdelhady, A. L.; Manna, L., **Zero-Dimensional Cesium Lead Halides: History, Properties, and Challenges.** *J. Phys. Chem. Lett.* **2018**, *9*, 2326-2337.

Akkerman, Q. A.; Rainò, G.; Kovalenko, M. V.; Manna, L., **Genesis, Challenges and Opportunities for Colloidal Lead Halide Perovskite Nanocrystals.** *Nat. Mater.* **2018**, *17*, 394-405.

Akkerman, Q. A.; Martínez-Sarti, L.; Goldoni, L.; Imran, M.; Baranov, D.; Bolink, H. J.; Palazon, F.; Manna, L., **Molecular Iodine for a General Synthesis of Binary and Ternary Inorganic and Hybrid Organic-Inorganic Iodide Nanocrystals.** *Chem. Mater.* **2018**, *30*, 6915-6921.

Akkerman, Q. A.; Bladt, E.; Petralanda, U.; Dang, Z.; Sartori, E.; Baranov, D.; Abdelhady, A.L.; Infante, I.; Bals, S.; Manna, L. **Fully Inorganic Ruddlesden Popper Double Cl-I and Triple Cl-Br-I Lead Halide Perovskite Nanocrystals.** Submitted

As contributor:

Palazon, F.; **Akkerman, Q. A.;** Prato, M.; Manna, L., **X-Ray Lithography on Perovskite Nanocrystals Films: From Patterning with Anion-Exchange Reactions to Enhanced Stability in Air and Water.** *ACS Nano* **2016**, *10*, 1224-1230.

Palazon, F.; Di Stasio, F.; Akkerman, Q. A.; Krahne, R.; Prato, M.; Manna, L., **Polymer-Free Films of Inorganic Halide Perovskite Nanocrystals as UV-to-White Color-Conversion Layers in LEDs.** *Chem. Mater.* **2016**, *28*, 2902-2906.

Srimath Kandada, A. R.; Neutzner, S.; D’Innocenzo, V.; Tassone, F.; Gandini, M.; **Akkerman, Q. A.;** Prato, M.; Manna, L.; Petrozza, A.; Lanzani, G., **Nonlinear Carrier Interactions in Lead Halide Perovskites and the Role of Defects.** *J. Am. Chem. Soc.* **2016**, *138*, 13604-13611.

Dang, Z.; Shamsi, J.; Palazon, F.; Imran, M.; **Akkerman, Q. A.**; Park, S.; Bertoni, G.; Prato, M.; Brescia, R.; Manna, L., **In Situ Transmission Electron Microscopy Study of Electron Beam-Induced Transformations in Colloidal Cesium Lead Halide Perovskite Nanocrystals.** *ACS Nano* **2017**, *11*, 2124-2132.

Palazon, F.; Almeida, G.; **Akkerman, Q. A.**; De Trizio, L.; Dang, Z.; Prato, M.; Manna, L., **Changing the Dimensionality of Cesium Lead Bromide Nanocrystals by Reversible Postsynthesis Transformations with Amines.** *Chem. Mater.* **2017**, *29*, 4167-4171.

Di Stasio, F.; Imran, M.; **Akkerman, Q. A.**; Prato, M.; Manna, L.; Krahn, R., **Reversible Concentration-Dependent Photoluminescence Quenching and Change of Emission Color in CsPbBr₃ Nanowires and Nanoplatelets.** *J. Phys. Chem. Lett.* **2017**, *8*, 2725-2729.

Palazon, F.; Urso, C.; De Trizio, L.; **Akkerman, Q.**; Marras, S.; Locardi, F.; Nelli, I.; Ferretti, M.; Prato, M.; Manna, L., **Postsynthesis Transformation of Insulating Cs₄PbBr₆ Nanocrystals into Bright Perovskite CsPbBr₃ through Physical and Chemical Extraction of CsBr.** *ACS Energy Lett.* **2017**, 2445-2448.

Meinardi, F.; **Akkerman, Q. A.**; Bruni, F.; Park, S.; Mauri, M.; Dang, Z.; Manna, L.; Brovelli, S., **Doped Halide Perovskite Nanocrystals for Reabsorption-Free Luminescent Solar Concentrators.** *ACS Energy Lett.* **2017**, 2368-2377.

Dang, Z.; Shamsi, J.; **Akkerman, Q. A.**; Imran, M.; Bertoni, G.; Brescia, R.; Manna, L., **Low-Temperature Electron Beam-Induced Transformations of Cesium Lead Halide Perovskite Nanocrystals.** *ACS Omega* **2017**, *2*, 5660-5665.

Lorenzon, M.; Sortino, L.; Akkerman, Q.; Accornero, S.; Pedrini, J.; Prato, M.; Pinchetti, V.; Meinardi, F.; Manna, L.; Brovelli, S., **Role of Nonradiative Defects and Environmental Oxygen on Exciton Recombination Processes in CsPbBr₃ Perovskite Nanocrystals.** *Nano Lett.* **2017**, *17*, 3844-3853.

Palazon, F.; Almeida, G.; **Akkerman, Q. A.**; De Trizio, L.; Dang, Z.; Prato, M.; Manna, L., **Changing the Dimensionality of Cesium Lead Bromide Nanocrystals by Reversible Postsynthesis Transformations with Amines.** *Chem. Mater.* **2017**, *29*, 4167-4171.

Almeida, G.; Goldoni, L.; **Akkerman, Q. A.**; Dang, Z.; Khan, A. H.; Marras, S.; Moreels, I.; Manna, L., **Role of Acid-Base Equilibria in the Size, Shape, and Phase Control of Cesium Lead Bromide Nanocrystals.** *ACS Nano* **2018**, *12*, 1704-1711.

Palazon, F.; Chen, F.; **Akkerman, Q. A.**; Imran, M.; Krahn, R.; Manna, L., **Effects of Oxygen Plasma on the Chemical, Light-Emitting, and Electrical-Transport Properties of Inorganic and Hybrid Lead Bromide Perovskite Nanocrystal Films.** *ACS Appl. Nano Mater.* **2018**, 5396-5400

Berends, A. C.; van der Stam, W.; **Akkerman, Q. A.**; Meeldijk, J. D.; van der Lit, J.; de Mello Donega, C., **Anisotropic 2D Cu_{2-x}Se Nanocrystals from Dodecaneselenol and Their Conversion to CdSe and CuInSe₂ Nanoparticles.** *Chem. Mater.* **2018**, *30*, 3836-3846.

Imran, M.; Ijaz, P.; Baranov, D.; Goldoni, L.; Petralanda, U.; **Akkerman, Q. A.**; Abdelhady, A. L.; Prato, M.; Bianchini, P.; Infante, I.; Manna, L., **Shape-Pure, Nearly Monodispersed CsPbBr₃ Nanocubes Prepared Using Secondary Aliphatic Amines.** *Nano Lett.* Article ASAP

Almeida, G.; Ashton, O. J.; Goldoni, L.; Maggioni, D.; Petralanda, U.; Mishra, N.; **Akkerman, Q. A.**; Infante, I.; Snaith, H. J.; Manna, L., **The Phosphine Oxide Route toward Lead Halide Perovskite Nanocrystals.** *J. Am. Chem. Soc.* **2018**, *140*, 14878-14886.

Pinchetti, V.; Anand, A.; **Akkerman, Q. A.**; Sciacca, D.; Lorenzon, M.; Meinardi, F.; Fanciulli, M.; Manna, L.; Brovelli, S. **Trap-Mediated Two-Step Sensitization of Manganese Dopants in Perovskite Nanocrystals.** *ACS Energy Lett.*, **2019**, 85–93

Publications prior to PhD:

van der Stam, W.; Gantapara, A. P.; **Akkerman, Q. A.**; Soligno, G.; Meeldijk, J. D.; van Roij, R.; Dijkstra, M.; de Mello Donega, C., **Self-Assembly of Colloidal Hexagonal Bipyramid- and Bifrustum-Shaped ZnS Nanocrystals into Two-Dimensional Superstructures.** *Nano Lett.* **2014**, *14*, 1032-1037.

van der Stam, W.; **Akkerman, Q. A.**; Ke, X.; van Huis, M. A.; Bals, S.; de Mello Donega, C., **Solution-Processable Ultrathin Size- and Shape-Controlled Colloidal Cu_{2-x}S Nanosheets.** *Chem. Mater.* **2015**, *27*, 283-291.

Akkerman, Q. A.; Genovese, A.; George, C.; Prato, M.; Moreels, I.; Casu, A.; Marras, S.; Curcio, A.; Scarpellini, A.; Pellegrino, T.; Manna, L.; Lesnyak, V., **From Binary Cu_2S to Ternary Cu-In-S and Quaternary Cu-In-Zn-S Nanocrystals with Tunable Composition Via Partial Cation Exchange.** *ACS Nano* **2015**, *9*, 521-531.

Akkerman, Q. A.; D'Innocenzo, V.; Accornero, S.; Scarpellini, A.; Petrozza, A.; Prato, M.; Manna, L., **Tuning the Optical Properties of Cesium Lead Halide Perovskite Nanocrystals by Anion Exchange Reactions.** *J. Am. Chem. Soc.* **2015**, *137*, 10276-10281.

page left blank intentionally

